Computational Mechanics (2026) 77:1267–1289
https://doi.org/10.1007/s00466-025-02706-1

ORIGINAL PAPER

GPU-accelerated multi-material FVM–SPH with immersed boundary method for high-fidelity modeling of shock–structure interactions

Jian-Yu Chen[1,2] · **Jidong Zhao**[1] · **Ruo-Feng Feng**[1] · **Rui-Chen Ni**[3] · **Chong Peng**[4]

Received: 26 May 2025 / Accepted: 23 September 2025 / Published online: 17 October 2025

Abstract

Shock wave propagation from explosive detonations and its damaging effects on adjacent structures involve complex compressible fluid flows and intense fluid–structure interactions (FSI), posing significant computational challenges. This paper proposes a novel GPU-accelerated hybrid framework that couples multi-material finite volume method (FVM) with smoothed particle hydrodynamics (SPH) to simulate the entire process of shock wave dynamics and structural response, including fracture propagation and fragmentation. The FVM efficiently resolves explosive detonation and shock propagation in fluids using a six-equation model with adaptive Riemann solvers, while SPH captures large structural deformations and material failure in a meshless Lagrangian framework. The immersed boundary method (IBM) enables robust two-way coupling between FVM and SPH domains, ensuring accurate momentum and energy transfer across fluid–structure interfaces. Leveraging GPU parallelization, the framework achieves high computational efficiency, enabling simulations with millions of nodes/particles. Five benchmark cases—shock–bubble interaction, 2D/3D underwater explosions, reinforced concrete damage under blast loads, and dynamic fracture of steel tubes—are used to validate the method. Simulation results show strong agreement with experimental data. The GPU acceleration achieves a 350 times speedup over CPU-based SPH, making the framework practical for large-scale FSI problems. This work demonstrates the unified FVM–SPH–IBM approach is capable of handling multi-material compressible flows, extreme structural deformations, and fragmentation, offering a powerful tool for defense and engineering applications.

Keywords Multi-material finite volume method · Smoothed particle hydrodynamics · Fracture and fragmentation · GPU · Shock wave

1 Introduction

The explosion of military weapons, involving shock wave propagation, fragmentation, and their impact on vehicles and personnel, is of critical importance in both national defense and engineering. These strong fluid structure interaction problems are highly nonlinear and complex, making them difficult to solve analytically. While experimental methods can be used to study such explosion problems, they are time-consuming and prone to human error, which can lead to inconsistent results. Therefore, developing a robust and efficient fluid–structure interaction solver for accurately predicting the behavior of compressible flows and the resulting damage to solid structures is essential for advancing both defense and engineering applications.

Several numerical studies have been conducted on the simulation of compressible fluid flow and its interaction with solid structures using conventional mesh-based

---

✉ Jian-Yu Chen
chenjianyu@njust.edu.cn

✉ Jidong Zhao
jzhao@ust.hk

[1] Department of Civil and Environmental Engineering, The Hong Kong University of Science and Technology, HKSAR, China

[2] School of Mechanical Engineering, Nanjing University of Science and Technology, 200 Xiaolingwei Street, Nanjing 210094, China

[3] Zhejiang Geely Holding Group Co., Ltd, Hangzhou 310000, China

[4] School of Civil Engineering, Southeast University, Nanjing 211189, China

methods [1–4]. For example, Wang et al. [5] presented a local Riemann solver for strongly nonlinear equations of state (EOS) such as the Jones–Wilkins–Lee (JWL) EOS and investigated the entire process of the detonation of the TNT and aluminized explosives. Saurel et al. [1] proposed efficient relaxation methods for interfaces separating compressible fluids, cavitating flows, and shocks in multiphase mixtures, demonstrating that the finite volume method (FVM) can efficiently capture two-phase flow. Chen et al. [4] used the finite element method (FEM) in LS-DYNA to simulate the expansion and dynamic fracture of cylindrical shells under blast loading, analyzing failure modes, fracture mechanisms, and fragment distribution of metal shells. Zakrisson et al. [3] performed numerical simulations of blast loads and structural deformation resulting from near-field explosions in air. However, when addressing explosion and impact problems involving large deformations, these mesh-based methods can suffer from mesh distortions, leading to issues such as mass loss, unphysically negative density, negative energy, or even computational failure. In contrast, meshless methods-such as the material point method (MPM) [6], smoothed particle hydrodynamics (SPH) [7], reproducing kernel particle method (RKPM) [8], and peridynamics [9–11]—have been proposed to better handle large deformation problems, avoiding the limitations of mesh-based approaches.

In this paper, the smoothed particle hydrodynamics (SPH) method is employed to investigate the dynamic behavior and damage characteristics of solid structures for several reasons. First, since the SPH method does not rely on a mesh, it is well-suited to handle large deformations in a pure Lagrangian framework. This allows for natural treatment of interfaces between different materials. Additionally, SPH makes it easy to implement complex constitutive models that account for new physical phenomena. Originally proposed by Monaghan [12] and Lucy [13], SPH has been successfully applied to free surface flow and granular flow problems. Over time, it has been extended to simulate high-velocity impacts and explosive detonation events. For example, Liu et al. [14] developed an SPH-based approach to model explosive detonation and shock wave propagation in water. Libersky et al. [15] used SPH to simulate the dynamic response of solid structures, including fracture and fragmentation, and to predict fracture patterns and mass distributions in metal shells. Feng et al. [16] modified SPH to simulate three-dimensional shaped charge detonations and the resulting damage to nearby steel slabs, showing that the method accurately captures the high-velocity metal jet and fragmentation of steel plates. Chen et al. [17, 18] has also developed a GPU-accelerated SPH solver for simulating 3D high-velocity impacts and soil explosion problems. This solver has been successfully applied to capture soil fragmentation [17, 18], shaped charge detonation [19], and non-ideal explosive detonation [20].

While mesh-based methods can accurately capture shock wave propagation in air, the SPH method encounters several challenges in this regard. First, modeling the air domain to capture shock wave propagation requires millions of SPH particles, which significantly increases computational time. Second, the large density ratio between air and the explosive gaseous products can lead to numerical instability or even computational termination. Third, mesh-based methods tend to be more accurate and computationally efficient than meshless methods in capturing shock wave propagation. As a result, some researchers have proposed hybrid approaches that combine mesh-based and particle methods to address fluid–structure interaction problems. For instance, Tsuji et al. [21] proposed a hybrid method that integrates SPH with mesh-based ALE (Arbitrary Lagrangian–Eulerian) schemes to simulate material fracture and cracking in high-explosive-driven experiments, using appropriate damage or failure models in SPH. Zhang et al. [22] developed a combined RKDG-FEM approach for simulating underwater explosion (UNDEX) problems involving shock–bubble–structure interactions and cavitation. Sun et al. [23] coupled the multi-resolution δ^{+}-SPH model with the Total Lagrangian SPH model to simulate the complex three-dimensional (3D) Fluid Structure Interaction (FSI) problems. Liu et al. [24, 25] proposed a novel smoothed-interface SPH multiphase model to simulate fiber orientation in blood vessels. These results show that the smoothed-interface SPH multiphase model can eliminate non-physical gaps at interfaces, greatly enhancing interface continuity and stability. Huang et al. [26] coupled the peri-dynamics (PD) with SPH for fracture analysis of fluid–structure interaction (FSI) problems. In our current work, we couple the mesh-based FVM method with the meshless SPH method to simulate the entire process of shock wave propagation and its interaction with solid structures. The multi-material FVM method is used to capture explosive detonation and shock wave propagation, while the SPH method predicts the dynamic behavior of solid structures. To transfer physical information between the fluid and solid domains, we use the immersed boundary method (IBM) developed by Peskin et al. [27] to couple the SPH and FVM approaches, enabling accurate simulations of fluid–structure interactions.

To significantly increase computational efficiency, the Compute Unified Device Architecture (CUDA) parallel computing platform and programming model developed by NVIDIA was employed in the FVM–SPH solver. Several researchers have previously employed GPUs within the SPH framework. For example, Hérault et al. [28] implemented an SPH solver for free surface flows on a graphical processing unit (GPU) using the CUDA platform, achieving substantial speed-ups. Mokos et al. [29] demonstrated the acceleration of a multi-phase SPH method using a GPU, enabling simulations with large particle numbers (10–20 million) on a single GPU card. Consequently, in our current research, the GPU parallel computing technique is applied to the multi-material FVM–SPH solver, harnessing the power of GPUs to dramatically enhance computational efficiency.

The paper is organized as follows: Sections 2 to 4 provide a brief introduction and solution procedure for the SPH and FVM methods. Section 5 presents five benchmark numerical cases, including shock–bubble interaction, two-dimensional underwater explosion in free field, underwater explosion near a steel plate, damage to a reinforced concrete slab under blast loading, and two-dimensional dynamic fracture of a steel tube under shock loading to validate the accuracy of the multi-material FVM–SPH method. Finally, the novelties and conclusions are summarized in Sect. 6.

2 Fundamentals of the SPH and FVM method

2.1 Function approximation in SPH

The SPH method is used for the prediction of the dynamic response of solid structures under blast and impact loads. The basic idea of the SPH method is to interpolate physical variables based on neighboring particles. The first step is the kernel approximation. An arbitrary field $\langle f(\boldsymbol{x})\rangle$ is written as a convolution with the smoothing function W.

$$\langle f(\boldsymbol{x})\rangle = \int_{\Omega} f(\boldsymbol{x'})W(\boldsymbol{x}-\boldsymbol{x'},h)d\boldsymbol{x'}. \tag{1}$$

The Wendland kernel function [30], which can mitigate tensile instability and particle penetration, is employed in the SPH method

$$W(q,h) = \alpha_d \begin{cases} \left(1-\frac{q}{2}\right)^4(2q+1) & 0 \le q < 2; \\ 0 & q \ge 2. \end{cases} \tag{2}$$

where the normalization constant $\alpha_d = 7/\left(4\pi h^2\right)$ in two dimensions and $\alpha_d = 21/\left(16\pi h^3\right)$ in three dimensions; $q = \frac{|\boldsymbol{x}|}{h}$ is the normalized distance. The smoothing length can be updated using the time derivative, as given by [14]. It follows that the support domain radius decreases as the density increases:

$$\frac{dh_i}{dt} = -\frac{1}{d}\frac{h_i}{\rho_i}\frac{d\rho_i}{dt}. \tag{3}$$

Afterwards, the integral form of an arbitrary physical variable is approximated using a summation over particles.

$$\langle f(\boldsymbol{x}_i)\rangle = \sum_{j=1}^{N} f(\boldsymbol{x}_j)W_{ij}\frac{m_j}{\rho_j}. \tag{4}$$

Based on the kernel approximation and particle approximation, the discretized form of the governing equation (Navier–Stokes) can be obtained as

$$\begin{cases} \frac{\mathrm{d}\rho}{\mathrm{d}t} = \sum_{j=1}^{N} m_j\left(\boldsymbol{v_i}-\boldsymbol{v_j}\right)\cdot\nabla_i W_{ij} & (a) \\ \frac{\mathrm{d}\boldsymbol{v}_i}{\mathrm{d}t} = \sum_{j=1}^{N} m_j\left(\frac{\boldsymbol{\sigma_i}+\boldsymbol{\sigma_j}}{\rho_i\rho_j}+\mathit{\Pi}_{ij}\boldsymbol{I}\right)\cdot\nabla_i W_{ij} & (b) \\ \frac{\mathrm{d}e_i}{\mathrm{d}t} = \frac{1}{2}\sum_{j=1}^{N} m_j\frac{p_i+p_j}{\rho_i\rho_j}\left(\boldsymbol{v_i}-\boldsymbol{v_j}\right)\cdot\nabla_i W_{ij}+\frac{1}{2\rho_i}\boldsymbol{S}_i\boldsymbol{\varepsilon_i} & (c) \\ p_i = p(\rho_i,e_i) & (d) \end{cases} \tag{5}$$

where ρ_i, m_i, v_i, e_i and p_i are the density, mass, velocity, energy, and pressure of particle i, respectively; $\mathit{\Pi}_{ij}$ is artificial viscosity; $\boldsymbol{\sigma}$ is stress tensor; $\boldsymbol{S}$ is deviatoric stress tensor; $\boldsymbol{\varepsilon_i}$ is the strain rate tensor.

In the SPH solver, the Monaghan type artificial viscosity [31] is employed to dampen numerical oscillations and prevent particles penetration,

$$\mathit{\Pi}_{ij} = \begin{cases} \frac{-\alpha c_{ij}\phi_{ij}+\beta\phi_{ij}^2}{\rho_{ij}}, & \boldsymbol{v_{ij}}\cdot\boldsymbol{x_{ij}} < 0; \\ 0, & \boldsymbol{v_{ij}}\cdot\boldsymbol{x_{ij}} \ge 0. \end{cases} \tag{6}$$

Here,$\phi_{ij} = \frac{h_{ij}\boldsymbol{v_{ij}}\cdot\boldsymbol{x_{ij}}}{|\boldsymbol{x_{ij}}|^2+(\varphi)^2}$,$c_{ij} = \frac{1}{2}(c_i+c_j)$,$\rho_{ij} = \frac{1}{2}(\rho_i+\rho_j)$, $h_{ij} = \frac{1}{2}(h_i+h_j)$, $\boldsymbol{v_{ij}} = \boldsymbol{v_i}-\boldsymbol{v_j}$, and $\boldsymbol{x_{ij}} = \boldsymbol{x_i}-\boldsymbol{x_j}$,

The boundary treatment is an important issue in the SPH method. In our current research, ghost particles are employed for the boundary treatment. The symmetrical boundary and fixed boundary are applied for the SPH particles within the solid domain. For the implementation of the symmetrical boundary, the velocity of a ghost particle tangent to the boundary (shear velocity) is set equal to that of the corresponding real particle, while the velocity component normal to the boundary is set to the negative of the velocity of the real particle. The stress tensor of the ghost particles is determined in accordance to the following relations [32].

$$\sigma_G^{\alpha\beta} = \begin{cases} \sigma_R^{\alpha\beta}, & \alpha = \beta; \\ -\sigma_R^{\alpha\beta}, & \alpha \neq \beta. \end{cases} \tag{7}$$

where $\sigma_R^{\alpha\beta}$ and $\sigma_G^{\alpha\beta}$ are the components of the stress tensor of the real particles and ghost particles, respectively. As for the fixed boundary implementation, the velocity components of three layers of the real particles near the physical bounday are determined as zero.

2.2 Multi-material finite volume method

2.2.1 Discretization of the governing equation

Since the main goal of this paper is to develop a coupled approach for the simulation of multiphase flow (explosive gaseous products and air medium)–structure interaction, the compressible Eulerian equation considering two different phases is employed [1]. Different volume fractions of different phases α_n should satisfy

$$\sum_{n=1}^{2} \alpha_n = 1. \tag{8}$$

This six equation model (Eq. 9) that can be used to determine different physical variables including fractions, densities, and energies of two phases can be obtained by substituting the fraction condition mentioned above (Eq. 8) to the continuity, momentum, and energy equation.

$$\frac{\partial \boldsymbol{U}}{\partial t} + \frac{\partial \boldsymbol{F}_1}{\partial x} + \frac{\partial \boldsymbol{F}_2}{\partial y} + \frac{\partial \boldsymbol{F}_3}{\partial z} = \boldsymbol{\phi}, \tag{9}$$

where

$$\begin{gathered} \boldsymbol{U} = \begin{pmatrix} \alpha_1\rho_1 \\ \alpha_2\rho_2 \\ \rho u \\ \rho v \\ \rho w \\ \rho E \end{pmatrix}, \boldsymbol{F}_1 = \begin{pmatrix} \alpha_1\rho_1 u \\ \alpha_2\rho_2 u \\ \rho u^2 + p \\ \rho uv \\ \rho uw \\ (\rho E + p)u \end{pmatrix}, \boldsymbol{F}_2 = \begin{pmatrix} \alpha_1\rho_1 v \\ \alpha_2\rho_2 v \\ \rho uv \\ \rho v^2 + p \\ \rho vw \\ (\rho E + p)v \end{pmatrix}, \\ \boldsymbol{F}_3 = \begin{pmatrix} \alpha_1\rho_1 w \\ \alpha_2\rho_2 w \\ \rho uw \\ \rho vw \\ \rho w^2 + p \\ (\rho E + p)w \end{pmatrix}, \boldsymbol{\phi} = \begin{pmatrix} 0 \\ 0 \\ f_x \\ f_y \\ f_z \\ f_x u + f_y v + f_z w \end{pmatrix}, \end{gathered} \tag{10}$$

in which, the pressure $p = \alpha_1 p_1 + \alpha_2 p_2$; The total energy $E = Y_1 e_1 + Y_2 e_2 + \frac{1}{2}\left(u^2 + v^2 + w^2\right)$; p_n and e_n are the pressure and energy of phase n, respectively. The mass fraction of phase n is $Y_n = \alpha_n \rho_n / \rho$; The total density $\rho = \alpha_1\rho_1 + \alpha_2\rho_2$. u, v, and w represent the velocities in the x, y, and z directions, respectively. The source terms $\boldsymbol{\phi}$ include body forces and external forces, such as gravity.

The flux derivative with respect to x, y, and z directions in Eq. (9) can be determined using the following equation,

$$\frac{\partial F}{\partial x} = \frac{\hat{F}_{i+\frac{1}{2},j,k} - \hat{F}_{i-\frac{1}{2},j,k}}{\Omega_{i,j,k}}, \tag{11}$$

in which, $\Omega_{i,j,k}$ is the volume of the element (i,j,k); $\hat{F}_{i+\frac{1}{2},j,k} = F_{i+\frac{1}{2},j,k} * S_{i+\frac{1}{2},j,k}$; $S_{i+\frac{1}{2},j,k}$ is the surface area of the element (i,j,k); The numerical flux $F_{i+\frac{1}{2},j,k}$ can be obtained based on U_L and U_R using the Riemann approximation solver. U_L and U_R can be obtained based on the MUSCL difference scheme, which can be referred to [33]. Additionally, in order to predict the explosive detonation and shock wave propagation in air and water medium, three different equation of states (EOSs), namely the ideal gas EOS, stiffened gas EOS, and the Jones-Wilkins-Lee (JWL) equation are employed in this work. For the ideal gas, the pressure is determined as

$$p = (\gamma - 1)\,\rho e\,, \tag{12}$$

in which, γ is a constant parameter. For the prediction of the high explosive detonation, the Jones-Wilkins-Lee (JWL) is used,

$$p = A\left(1 - \frac{w}{R_1 v}\right) e^{-R_1 v} + B\left(1 - \frac{w}{R_2 v}\right) e^{-R_2 v} + w\rho e\,, \tag{13}$$

in which, A, B, w, R_1, and R_2 are constant parameters. For the numerical prediction of underwater explosin, the siffened gas equation, which accounts for both the pressure-volume-temperature relationship and the internal energy associated with the material's "stiffness" (the resistance to compression), is employed,

$$p = (\gamma - 1)\,\rho e - P_c\,, \tag{14}$$

where γ and P_c are constant parameters. It should be noted that, there are only nine equations that include one volume fraction condition (Eq. 8), three EOSs (Eqs. 14 and 13), and six equations in the governing equation (Eq. 9) to solve eleven physical variables (α_1, α_2, ρ_1, ρ_2, p_1, p_2, e_1, e_2, u, v, and w). Consequently, three different equations are required to be added for the closure of the governing equation.

$$\begin{cases} \frac{\partial \alpha_1}{\partial t} + \nabla\cdot(\alpha_1 \boldsymbol{v}) - \alpha_1 \nabla\cdot\boldsymbol{v} = \mu\,(p_1 - p_2)\,; \\ \frac{\partial \alpha_1\rho_1 e_1}{\partial t} + \nabla\cdot(\alpha_1\rho_1 e_1 \boldsymbol{v}) - \alpha_1 p_1 \nabla\cdot\boldsymbol{v} = -p_I\mu\,(p_1 - p_2)\,; \\ \frac{\partial \alpha_2\rho_2 e_2}{\partial t} + \nabla\cdot(\alpha_2\rho_2 e_2 \boldsymbol{v}) - \alpha_2 p_2 \nabla\cdot\boldsymbol{v} = p_I\mu\,(p_1 - p_2)\,, \end{cases} \tag{15}$$

where p_I is the pressure of different phases; The pressure relaxation rate $\mu = \infty$. The key aspect of the two-phase FVM method is solving the transport equation using operator splitting. The first step involves solving the transport equation with the HLLC approximate Riemann solver, without considering the pressure equilibrium between the two phases. Following this, Newton's iteration method is applied to solve for the equilibrium pressure. The computation details of solving the transport equation will be elaborated in the following sections. At the end, the third-order Runge–Kutta method is used to update physical variables in the governing equation,

$$\begin{cases} \boldsymbol{U}^{(1)} = (\boldsymbol{I} + \Delta t \mathcal{L})\boldsymbol{U}^{n}; \\ \boldsymbol{U}^{(2)} = 3/4\boldsymbol{U}^{n} + 1/4(\boldsymbol{I} + \Delta t \mathcal{L})\boldsymbol{U}^{(1)}; \\ \boldsymbol{U}^{n+1} = 1/3\boldsymbol{U}^{n} + 2/3(\boldsymbol{I} + \Delta t \mathcal{L})\boldsymbol{U}^{(2)}. \end{cases} \tag{16}$$

where $\boldsymbol{I}$ is the identity matrix; the operator $\mathcal{L}(\boldsymbol{U}) = \frac{\partial \boldsymbol{U}}{\partial t} = -\left(\frac{\partial \boldsymbol{F}_1}{\partial x} + \frac{\partial \boldsymbol{F}_2}{\partial y} + \frac{\partial \boldsymbol{F}_3}{\partial z}\right) + \boldsymbol{\phi}$.

2.2.2 The HLLC approximate Riemann solver

The HLLC scheme [34] considering the contact and shear waves for solving the Riemann problem approximately is employed in the FVM solver. The HLLC approximation Riemann solver can be used to find approximations to the flux function directly. Figure 1 shows the structure of approximate solution of the Riemann problem in Eq. (17).

$$\boldsymbol{U}(x,t) = \begin{cases} \boldsymbol{U}_L & 0 \le S_L; \\ \boldsymbol{U}_{*L} & S_L \le 0 \le S_*; \\ \boldsymbol{U}_{*R} & S_* \le 0 \le S_R; \\ \boldsymbol{U}_R & 0 \ge S_R \end{cases} \tag{17}$$

where S_L, S_R, and S_* are speed of the left-moving shock, right-moving shock, and contact discontinuity, respectively. $\boldsymbol{U}_L$ and $\boldsymbol{U}_R$ are left and right states before the wave interaction. $\boldsymbol{U}_{*L}$ and $\boldsymbol{U}_{*R}$ are left and right intermediate states. The solution vector in the Star Region in the HLLC approximate Riemann solver is determined as,

$$\boldsymbol{U}_{*K} = \rho_k \left(\frac{S_k - u_k}{S_k - S_*}\right) \begin{pmatrix} 1 \\ S_* \\ v_K \\ w_K \\ \frac{E_K}{\rho_K} + (S_* - u_K)\left[S_* + \frac{p_K}{\rho k(S_K - \rho_K)}\right] \end{pmatrix}, \tag{18}$$

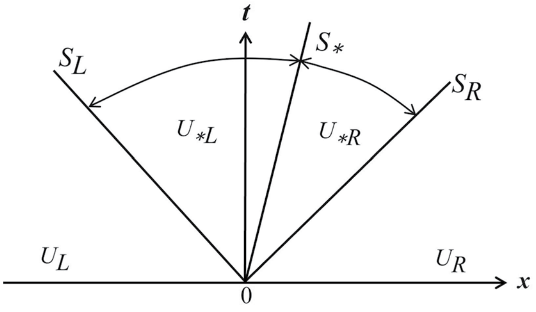

Fig. 1 The structure of the approximation of the Riemann problem

where $K = L$ or $K = R$. Therefore, the fluxes $\boldsymbol{F}_{*L}$ and $\boldsymbol{F}_{*R}$ can be completely determined using the following equation,

$$\boldsymbol{F}^{hllc}_{i+\frac{1}{2}} = \begin{cases} \boldsymbol{F}_L & 0 \le S_L; \\ \boldsymbol{F}_{*L} = \boldsymbol{F}_L + S_L(\boldsymbol{U}_{*L} - \boldsymbol{U}_L) & S_L \le 0 \le S_*; \\ \boldsymbol{F}_{*R} = \boldsymbol{F}_R + S_R(\boldsymbol{U}_{*R} - \boldsymbol{U}_R) & S_* \le 0 \le S_R; \\ \boldsymbol{F}_R & 0 \ge S_R \end{cases} \tag{19}$$

Davis [35] suggested the simple estimate for wave speed S_L and S_R in the solution of the Riemann problem directly,

$$\begin{aligned} S_L &= \min\{u_L - a_L, u_R - a_R\}, \\ S_R &= \max\{u_L + a_L, u_R + a_R\}. \end{aligned} \tag{20}$$

where a_L and a_R are sound speeds. In consequence, the S_* can be determined based on the wave speed S_L and S_R,

$$S_* = \frac{p_R - p_L + \rho_L u_L (S_L - u_L) - \rho_R u_R (S_R - u_R)}{\rho_L (S_L - u_L) - \rho_R (S_R - u_R)} \tag{21}$$

The mixture sound speed can be calculated as,

$$a_f^2 = Y_1 a_1^2 + Y_2 a_2^2 \tag{22}$$

in which a_1 and a_2 are sound speeds of different materials. The sound speed in a material can be determiend based on the partial derivative of pressure with respect to the density using an equation of state (EOS). In consequence, for the sound speed of explosive detonation, a is given by the relationship,

$$a_k^2(\rho_k, p) = \left(\frac{\partial p}{\partial \rho_k}\right)_s = \left(\frac{\partial p}{\rho_k}\right)_e + \frac{p}{\rho_k^2}\left(\frac{\partial p}{\partial e_k}\right)_\rho \tag{23}$$

The subscript s indicates that the derivative is taken at constant entropy (isentropic condition). The term $\left(\frac{\partial p}{\partial e_k}\right)_\rho$ accounts for the energy dependence of pressure. The equation of the sound speed of an ideal gas is [36],

$$a_k^2 = \gamma_k \frac{p}{\rho_k} \tag{24}$$

Following the wave speeds, the physical variables in the star region $(\alpha_n)_{*K}$, $(\rho_n)_{*K}$ and $(e_n)_{*K}$ can also be determined using the following relations,

$$(\alpha_n)_{*K} = (\alpha_n)_K \tag{25}$$

$$(\rho_n)_{*K} = (\rho_n)_{*K} \frac{S_K - u_K}{S_K - S_*} \tag{26}$$

$$(e_n)_{*K} = \mathrm{EOS}_n\left\{(\rho_n)_{*K}, (p_n)_K\right\} \tag{27}$$

Consequently, the solution vector $(\alpha_1 \boldsymbol{v}, \alpha_1\rho_1 e_1 \boldsymbol{v}, \alpha_2\rho_2 e_2 \boldsymbol{v})$ in the star region for the transport equation (Eq. (15)) can be determined from the intermediate states $(\alpha_n)_{*K}$, $(\rho_n)_{*K}$ and $(e_n)_{*K}$. Similarly, the third-order Runge–Kutta method can be used to update fractions α_n, energies of the different phases e_n in Eq. (15).

2.2.3 Iteration

Subsequently, the relaxation method is applied to ensure pressure equilibrium in the transport equation (Eq. 15) [1]. This relaxation step is crucial for maintaining pressure equilibrium at the multimaterial interface within the FVM method. The input parameters include the densities and phase fractions of the different materials. To solve for the phase fractions and energies, Newton's iteration method can be employed, as described in Eq. (28).

$$\begin{cases} e_n(\rho_n, p) - e_n^0\left(\rho_n^0, p_n^0\right) + p\left(\frac{1}{\rho_n} - \frac{1}{\rho_n^0}\right) = 0; \\ \sum_{n=1}^{2} \dfrac{C_n}{\rho_0} = 1\ , \end{cases} \tag{28}$$

in which, $C_n = \alpha_n\rho_n$ is a constant during the iteration process. e_n^0, ρ_n^0, and p_n^0 represent values before the iteration. In order to consider the conservation of energy, the pressure should be initialized by considering fluids governed by EOS again.

$$p^{eq} = \frac{\rho e - \left[\sum_{n=1}^{2} \alpha_n g_n(\rho_n)\right]}{\sum_{n=1}^{2} \alpha_n f_n(\rho_n)}. \tag{29}$$

$f_n(\rho_n)$ and $g_n(\rho_n)$ are functions of density that depend on the material properties in a Mie-Grüneisen-type equation of state (EOS): $\rho e = f_n(\rho_n)p + g_n(\rho_n)$. Once the mixture pressure is determined, the internal energies of the different phases are reinitialized with the help of their respective EOS before going to the next time step,

$$e_n(\rho_n, p^{eq}) = \frac{f_n(\rho_n)p^{eq} + g_n(\rho_n)}{\rho_n}. \tag{30}$$

Once the relaxed pressure in found, the corresponding fractions, densities, and energy for each phase can be determined.

3 Coupling of the FVM and SPH method

The coupling of the FVM and the SPH method is an important issue in the fluid–structure interaction problems. In our current research, the immersed boundary method is employed to handle the fluid–structure interface and transfer physical information between the solid domain and fluid domain. First, as shown in Fig. 2, the computational domain must be divided into three distinct regions: the fluid region, the solid region, and the fluid–structure interface. The pure fluid region and the pure solid region are treated using the two-phase FVM solver and the SPH solver, respectively.

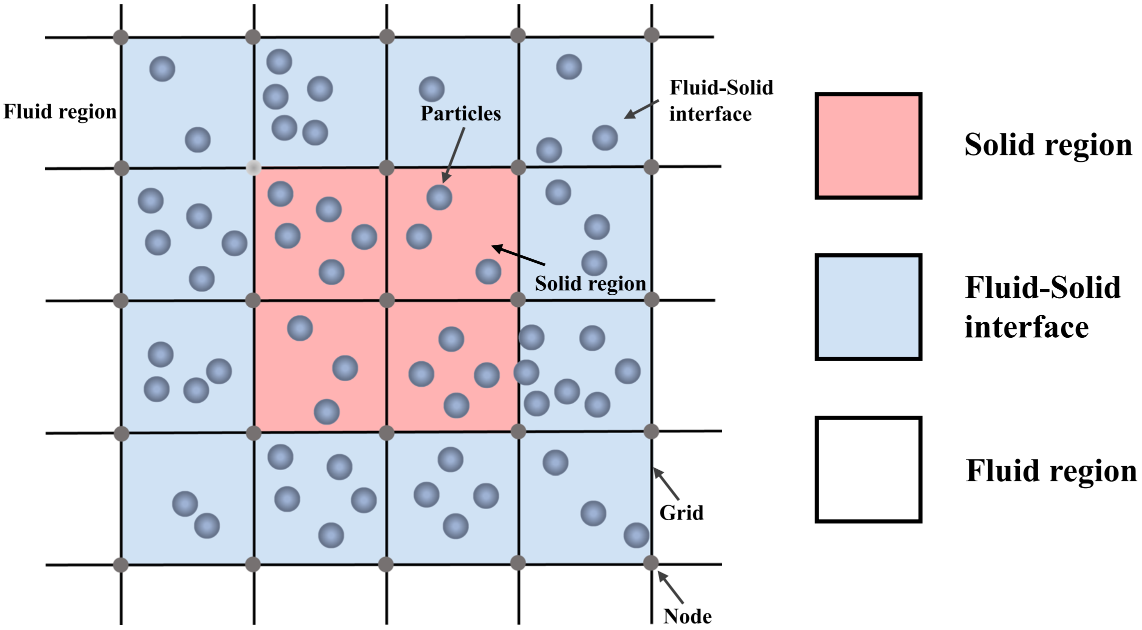

Fig. 2 Classification of three different regions: fluid region, solid region, and fluid–structure interface in the developed FVM–SPH method

More details with regards to the classification of three different regions can be referred to [33]. For the multi-material interface between the solid and fluid domains, the velocity of the interface node $\boldsymbol{v}_c^{ib}$ is interpolated based on the velocities of the particles $\boldsymbol{v}_i$ within the corresponding cell.

$$\boldsymbol{v}_c^{ib} = \sum_{i=1}^{N} \frac{1}{N}\boldsymbol{v}_i. \tag{31}$$

All of the other physical variables ψ_I of the nodes on the multi-material interface can be obtained based on the value of the quantity ψ_N at neighboring node N.

$$\psi_I = \frac{\sum w(d_N)\psi_N}{\sum w(d_N)}. \tag{32}$$

$w(d_N)$ is a weighting function, typically based on the distance d_N between points N and I. The closer N is to I, the higher the weight. Correspondingly, based on the conservation of momentum, the external forces acting on the SPH particles can be derived from the numerical flux increments [33].

$$\begin{aligned} \boldsymbol{f}_i^k =& -\frac{\left(\Delta\left(\rho\boldsymbol{v}\right)\right)_c^k - \boldsymbol{v}_c^{ib}\left(\Delta\rho\right)_c^k}{\Delta t} \\ =&\alpha^k\left(\boldsymbol{v}_c^{ib}\mathrm{RHS}_c^k\left(\rho\right) - \mathrm{RHS}_c^k\left(\rho\boldsymbol{v}\right)\right)\ , \end{aligned} \tag{33}$$

where $\mathrm{RHS}_c^k\left(\rho\right)$ and $\mathrm{RHS}_c^k\left(\rho\boldsymbol{v}\right)$ are increments of the mass flux and momentum flux, respectively. The external force exerted on each SPH partcle is determined as

$$\mathcal{F}_i^k = \frac{1}{n_c}\boldsymbol{f}_i^k V_c. \tag{34}$$

where n_c is the total number of particles in one cell; V_c is the volume of each cell. The total external force exerted on each SPH particle can be determined based on the third-order Runge–Kutta method [33],

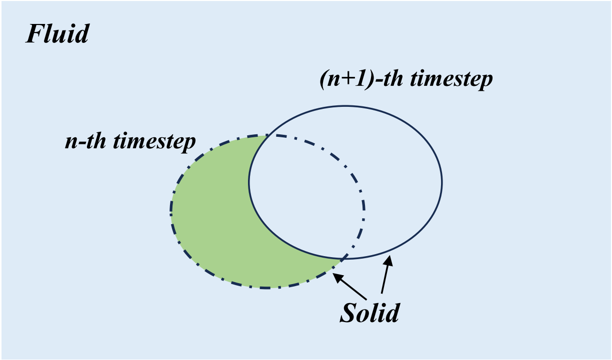

Fig. 3 Treatment of the physical variables of the moving structures

$$\mathcal{F}_i = \frac{1}{6}\mathcal{F}_i^1 + \frac{2}{3}\mathcal{F}_i^2 + \mathcal{F}_i^3. \tag{35}$$

This approach can be applied to ensure the accuracy of the velocity boundary implementation and the conservation of the momentum equation.

Additionally, as shown in Fig. 3, in simulations involving fluid–structure interaction with a moving structure, a solid node (located in the solid domain) may transition into a fluid node (within the fluid domain) at a given timestep directly. While it is unnecessary to interpolate physical variables within the solid region at the nth time step, a different approach is required when this region is converted to fluid. If the solid region (shaded green in Fig. 3) is directly converted to fluid at the (n+1)th step, its physical variables cannot be updated using the standard fluid integration method. Therefore, these variables must be initialized through direct interpolation. In such cases, all physical variables ψ associated with the fluid node-originating from the solid node in the previous timestep-should be consistently interpolated. This includes velocity components and other relevant variables, and the interpolation should be performed using the neighboring nodes, as described in Eq. (32).

4 Solution procedure of the FVM–SPH method

The solution procedure for the GPU-accelerated FV-SPH method is summarized as follows. The main steps of the multi-material FVM are illustrated in Fig. 4. Initially, all data are stored in the CPU memory and then transferred to the GPU memory for computation.

The first step in the GPU computation is the classification of three distinct regions: the fluid region, solid region, and the fluid–solid interface. The next step involves handling the physical and immersed boundaries. The velocity of the immersed boundary nodes is interpolated based on the velocities of the SPH particles in their corresponding cells. Other physical variables are interpolated using the neighboring nodes. The MUSCL scheme is applied as the difference scheme to determine U_R and U_L. The HLLC Riemann approximate solver is then used to compute the numerical flux based on U_R and U_L. To update the physical variables, the third-order Runge–Kutta integration method is employed. Finally, Newton's iteration method is used to reinitialize the equilibrium pressure, volume fractions, densities, and internal energies of the different phases, ensuring energy conservation and pressure equilibrium between the two phases. The external forces acting on the SPH particles are calculated based on the mass flux increments between the two different phases. The SPH method is then used to

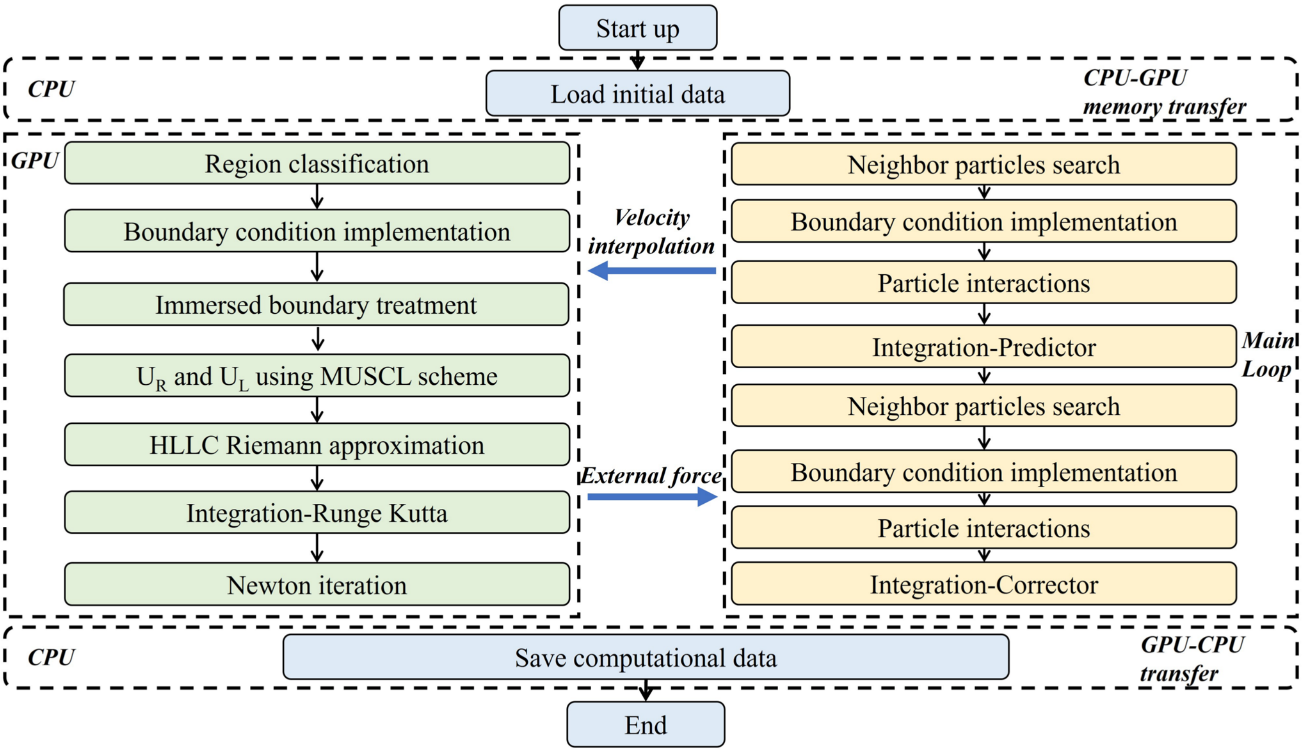

Fig. 4 Solution procedure of the multi-material FVM–SPH method

predict the dynamic behavior of solid structures. Once the numerical results are obtained, they are transferred from the GPU back to the CPU for occasional data storage.

5 Numerical examples

In this section, numerical simulations of five benchmark problems are presented to verify the accuracy of the GPU-accelerated multi-material FVM–SPH method. These problems include: shock–bubble interaction, two-dimensional underwater explosions in a free field, three-dimensional underwater explosions near steel structure, damage to reinforced concrete slabs under blast loading, and the dynamic fracture of steel tubes under shock loading. Since the single SPH solver has already been validated in our previous research through high-velocity impact and explosive detonation benchmarks [19], this study focuses solely on the verification of the multi-material FVM solver and the coupling of SPH and FVM. All of the numerical cases are executed on a single GeForce RTX 4090 Graphics Card.

5.1 Shock–bubble interaction

Firstly, the simulation of the two-dimensional shock–bubble interaction problem was performed to validate the accuracy of the multi-material finite volume method. This numerical simulation replicates the experimental work of Haas and Sturtenment [37–39], where a planar shock wave with a Mach number of 1.5 propagates into air at atmospheric conditions and interacts with a helium bubble. The primary objective of the experiment [37–39] is to investigate how the shock wave, propagating through a random medium, affects the structure of the mixing fluid flow.

The initial schematic of the computational domain is shown in Fig. 5. The dimensions of the computational domain are 325 × 89, and the dimensionless radius of the helium bubble (highlighted in red) is 25. The initial physical conditions for the air and helium regions are summarized in Eq. (36). The computational mesh has an initial size of 0.25, with a total of 939,322 nodes used in the simulation. The following boundary conditions are applied to the flow domain: the top and bottom boundaries are treated as solid walls with a standard reflecting boundary condition, the left boundary is set as a non-reflecting boundary, and the right side has specified inflow conditions based on the exact flow parameters. The ideal gas equation of state (EOS) is used to compute the pressure for both the helium and air media. The values of the adiabatic index, γ, for the air and helium are 1.4 and 1.67, respectively.

$$(\rho, u, v, p, \gamma) = \begin{cases} (1, 0, 0, 1.0, 1.4)\,, \text{for air}\;; \\ (1.3764, -0.394, 0, 1.5698, 1.4)\,, \text{for shock wave;} \\ (0.138, 0, 0, 10.8, 1.67)\,, \text{for helium bubble.} \end{cases} \tag{36}$$

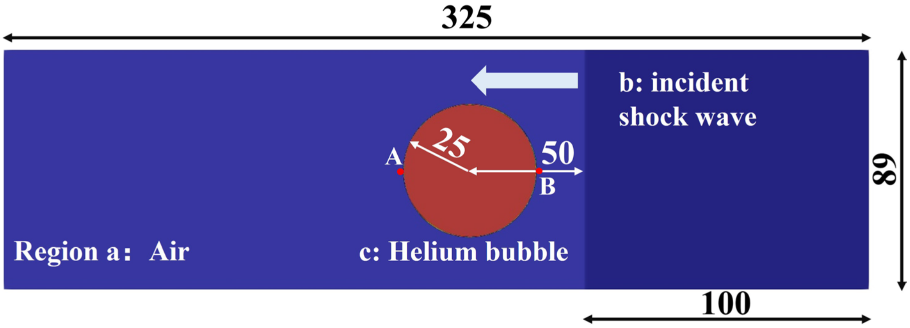

Fig. 5 The initial configuration of the 2D shock–bubble interaction, in which region a, region b, and region c are air at atmosphere condition, shock wave, and helium bubble, respectively. All of the lengths are dimensionless

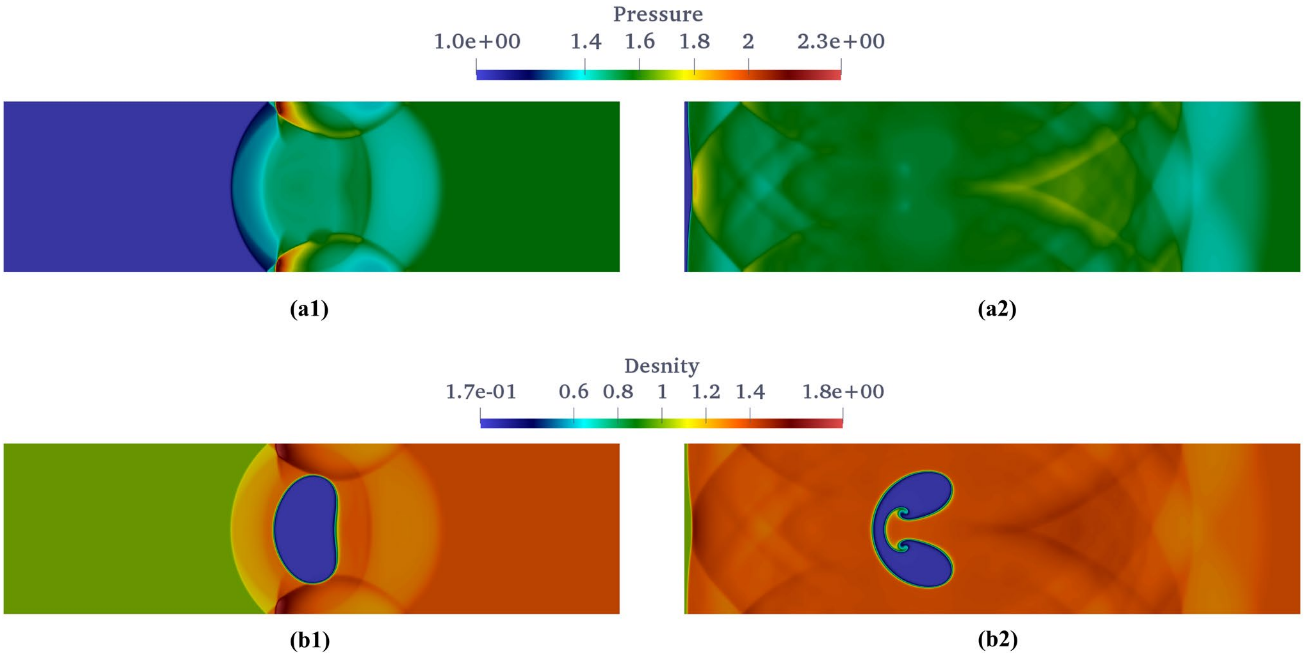

Fig. 6 Temporal evolution of the pressure and density distributions for shock bubble interaction at different times 67.6 and 180.4 μs

The pressure and density distributions from the 2D shock–bubble interaction problem, obtained using the multi-material FVM solver at different times 67.6 and 180.4 μs, are shown in Fig. 6. Initially, the shock wave propagates freely toward the helium bubble. Upon impact, a reflected shock wave and a refracted shock wave are generated. As shown in Fig. 7, a series of numerical schlieren images at different times 62, 82, 245, and 257 μs are compared to experimental shadowgraphs from [37, 39]. After the incident shock wave hits the helium bubble, a curved reflected shock wave forms outside the bubble, while a refracted shock wave propagates within the bubble. This behavior occurs because the sound speed in helium is higher than that in the surrounding air. The change in shape is further influenced by the vorticity generated at the bubble's edge. Over time, the bubble adopts a kidney-shaped form and spreads laterally.

The *x*-*t* path of the typical points for the shock wave interaction with the helium bubble in shown in Fig. 8. Note that the measured flow features move more or less in a constant velocity. Table 1 shows the comparison of the corresponding numerical velocities of the upstream edge V_{di} and downstream edge V_j of the helium bubble derived from Fig. 8 for the He cylinder case obtained from the FVM–SPH solver with those measured experimentally by Haas and Sturtevant [37]. It can be found that all of the relative errors are less than 10%. This numerical case demonstrates that the GPU-accelerated FVM method is highly effective at capturing the dynamics of multi-phase flow.

Additionally, as shown in Table 2, the computational efficiency of the multi-material FVM method is evaluated using the 2D shock–bubble interaction case. As the number of nodes increases, the computational time grows gradually from 40.0 to 1520.0 s. Despite this, the frames per second (FPS) for the simulation with 3,750,642 nodes remains high, demonstrating that the GPU-accelerated FVM method is effective for efficiently simulating two-phase flows. Moreover, the computational efficiency of the GPU-accelerated SPH method has been extensively examined in our

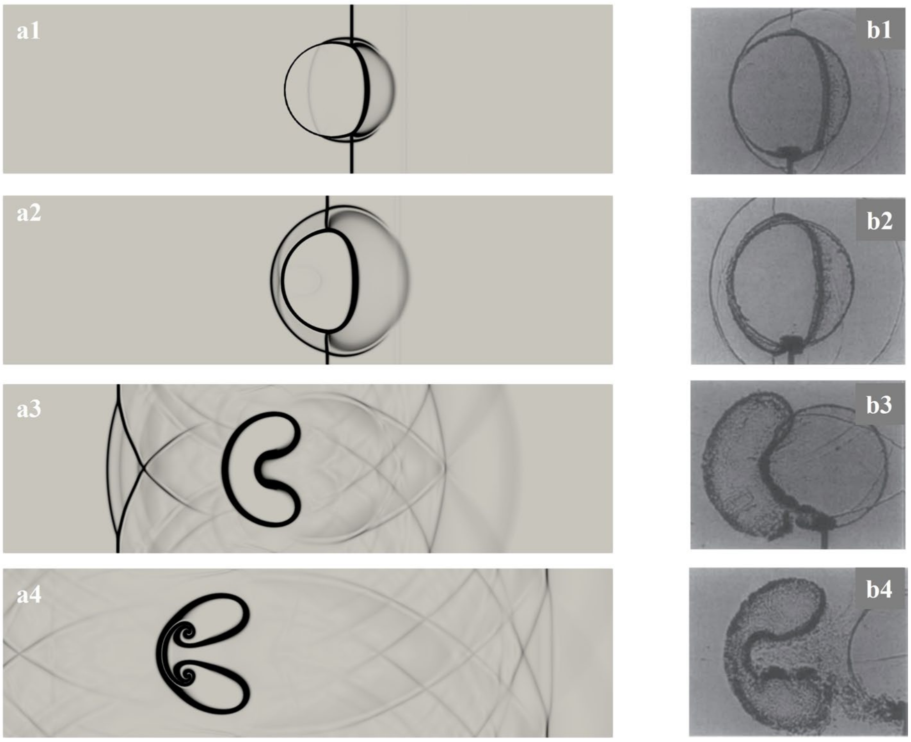

Fig. 7 Comparison of the (a1–a4) numerical schlieren of density distribution of shock–bubble interaction at different times with the (b1–b4) experimental data obtained from [37]

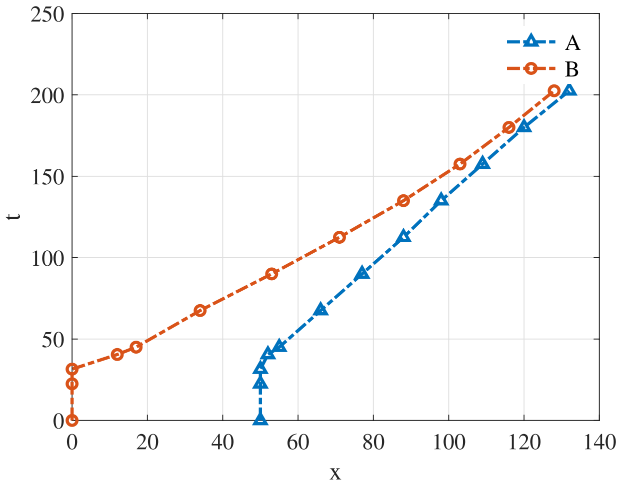

Fig. 8 *x-t* diagram for the typical points A and B, namely the upstream and downstream edges of the helium bubble

Table 1 A comparison of the numerical velocities of the upstream V_{di} and downstream edges V_j of the helium bubble obtained from the FVM–SPH solver with those measured experimentally by Haas and Sturtevant [37]

Velocity (ms^{-1})	Computation	Experiment	Discrepancy (%)
V_{di}	154	145	6.2
V_j	252	230	9.5

previous work, which focused on sand collapse and shaped charge detonation scenarios [19, 40]. It was found that the GPU-accelerated SPH method is 350 times faster than the sequential SPH code [19, 40]. In summary, fluid–structure interaction (FSI) problems can be efficiently addressed using the GPU-accelerated FVM–SPH method.

Table 2 Computational efficiency of the GPU-accelerated FVM–SPH solver for the shock–bubble interaction in 100 timesteps

Case	Node size	Nodes number	FPS (s^{-1})	T (s)
1	1.0	59,332	174.0	40.0
2	0.5	235,661	64.6	161.0
3	0.25	939,322	14.40	569.0
4	0.125	3,750,642	4.30	1520.0

5.2 Two-dimensional underwater explosion in a free field

In this section, we simulate a two-dimensional underwater explosion in a free field, a scenario also examined in [22, 36], to validate the effectiveness of this compressible multiphase algorithm for underwater explosions. As shown in Fig. 9, the computational domain spans $(x, y) \in [-1, 1] \times [-1, 1]$, with a mesh size of 0.0005 mm, resulting in a total of 321,602 nodes in the simulation. The initial physical conditions and parameters for both the water and explosive are summarized in Eq. (37). The ideal gas equation of state (EOS) is used to model the gaseous products, while the stiffened gas EOS is employed to describe the motion of the water. The constant parameters of the stiffened gas EOS for the water medium γ and P_c are 4.4 and 6.0 $\times 10^8$ Pa, respectively. All boundaries of the 2D underwater explosion are treated as non-reflecting boundaries.

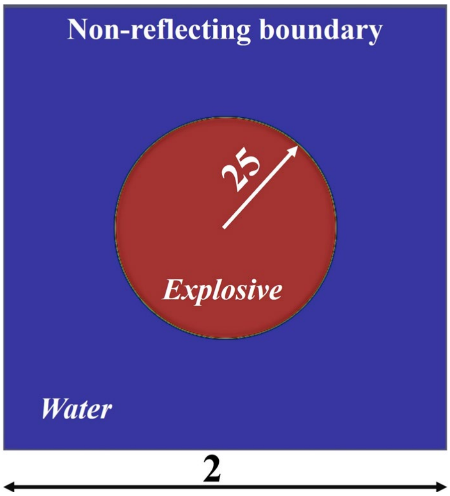

Fig. 9 Initial configuration of the 2D underwater explosion in a free field. All of the dimensions are in mm

$$(\rho, u, v, p, \gamma) = \begin{cases} (1000, 0, 0, 1.0 \times 10^5, 7.15)\,, \text{for water;} \\ (1630, 0, 0, 7.81 \times 10^9, 1.4)\,, \text{for bubble.} \end{cases} \tag{37}$$

The numerical prediction of pressure distribution from the underwater explosion at different times—0.01, 0.05, 0.1, and 0.15 ms—is shown in Fig. 10. Following the ignition of the TNT explosive, the shock wave propagates through the water medium. By around 0.14 ms, the shock wave reaches the boundary of the fluid domain. Additionally, the numerical data for pressure, velocity, and density distributions at the cross-section $y = 0$ along the x-axis at time $t = 0.0001$ s is compared with the exact solution of the problem as presented in [22] (Figs. 11, 12, 13). The comparison shows that the distributions of pressure, density, and velocity are generally in agreement with the analytical results from [22]. The discrepancies observed in the numerical results are primarily due to the use of different equations of state (EOS). For instance, the density magnitude in the interval $[-0.75, -0.4]$ is higher than that reported in [22]. The stiffened gas EOS is used in our calculation of water pressure in the underwater explosion, while Tait's EOS is used in [22]. The Tait EOS is designed for fluids like water, which are weakly compressible. Compared with the Tait EOS, the stiffened gas EOS is more suitable to address compressible fluid flows with high-pressure, high-temperature, such as underwater explosions. In conclusion, the numerical results demonstrate that the GPU-accelerated FV-SPH method effectively captures shock wave propagation and explosive dynamics in underwater explosions.

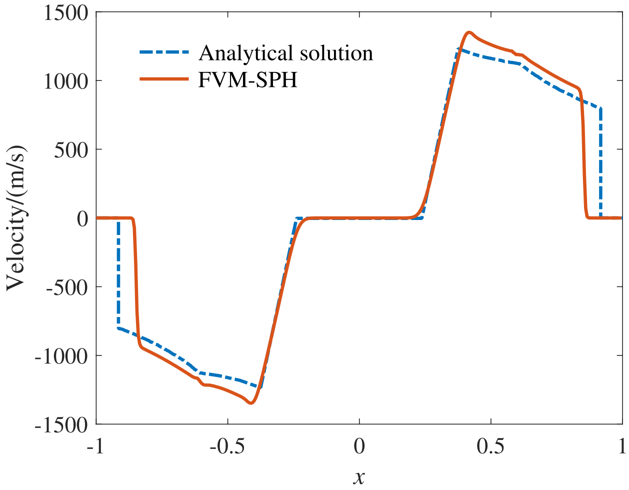

Fig. 11 Spatial distribution of the velocity of underwater explosion

5.3 3D Underwater explosion near steel plate

To validate the effectiveness of the developed FVM–SPH solver in simulating structural damage caused by 3D underwater explosions, and to further investigate the flow characteristics and dynamic behavior of metal structures, the underwater explosion near steel plate is simulated. The initial geometry of the underwater explosion near cylindrical steel structure is shown in the Fig. 14, which is identical to the numerical configuration in [22]. The dimensions of

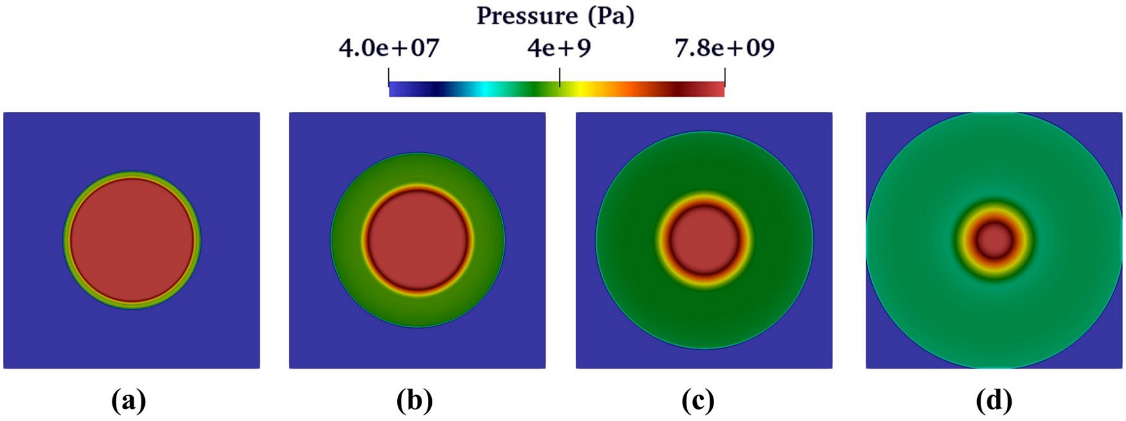

Fig. 10 Temporal evolution of the pressure distribution of the two-dimensional underwater explosion at different times 0.01, 0.05, 0.1, and 0.15 ms

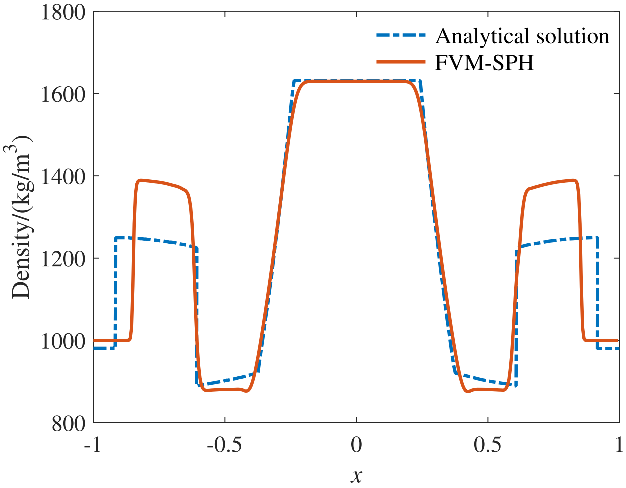

Fig. 12 Spatial distribution of the density of underwater explosion

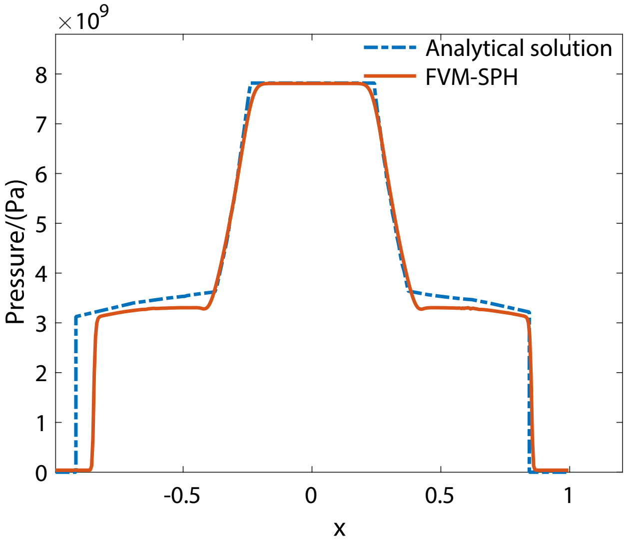

Fig. 13 Spatial distribution of the pressure of underwater explosion

the computational domain are 10.0 m × 10.0 m × 12.0 m. The distance between the center of the explosive and the bottom surface of the steel structure is 2.0 m. The diameter of this spherical explosive is 0.5 m, and the thickness of the steel plate is 0.068 m. The initial pressure of the explosive gaseous product is set as 6 GPa. The parameters for the Johnson-Cook constitutive model and EOS of the steel plate are listed in Tables 3 and 5, respectively. The initial mesh size is 0.0625 m. The initial particle spacing is 0.017 m, and a total of 815,131 partcles are involved in this simulation. All of the boundary conditions for the fluid domain are set as outlet boundaries, and the boundary of the steel structure is fixed.

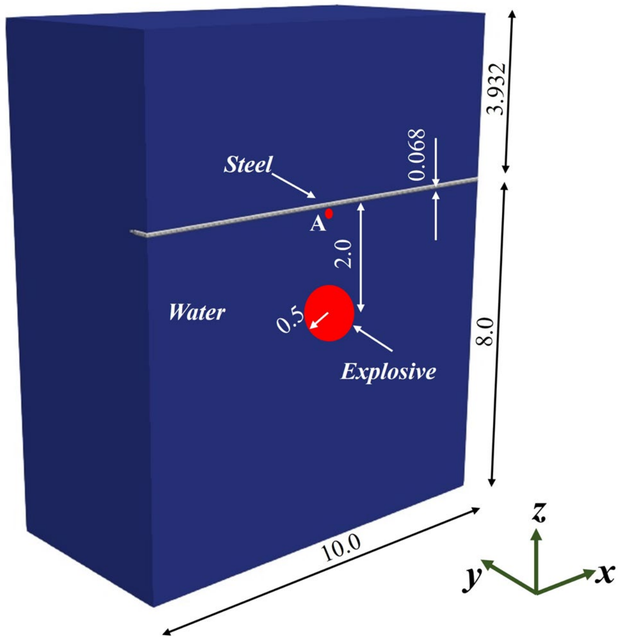

Fig. 14 Initial configuration of the damage of the steel plate subjected to the underwater explosion. All of the dimensions are in m

Firstly, we investigated the shock wave propagation in the water medium induced by the underwater explosion. The temporal evolution of the pressure contours and velocity distribution at various times (0.4, 1.6, and 2.4 ms) is shown in Fig. 15. It is observed that the shock wave reaches the bottom surface of the steel plate at 0.6 ms, where it undergoes both reflection and refraction. Part of the shock wave subsequently propagates through the steel plate. As a result of the transfer of internal energy from the explosive to the kinetic energy of the steel plate, the velocity of the plate increases gradually. Furthermore, the temporal evolution of the pressure at a typical point A (see Fig. 14) is depicted in Fig. 16. The pressure obtained from the GPU-accelerated FVM–SPH solver rapidly reaches its peak value of 0.82 GPa at 0.63 ms, after which it gradually decreases. The temporal evolution of the pressure from the FVM–SPH is generally consistent with the numerical results from the RKDG-FEM method [22], with the exception of the peak pressure. This discrepancy is likely due to the use of different equations of state (EOSs) for modeling the water medium—specifically, the stiffened gas EOS in the FVM–SPH solver versus Tait's EOS in the RKDG-FEM method.

The components of the stress tensor distribution of the steel structure caused by the underwater explosion at 5.0 ms are shown in Fig. 17. It is observed that the stress tensor

Table 3 Johnson-Cook model parameters of steel [22]

A (MPa)	B (MPa)	C	n	k	T_{room} (K)	T_{melt} (K)
950	560	0.014	0.26	1.03	273	1793

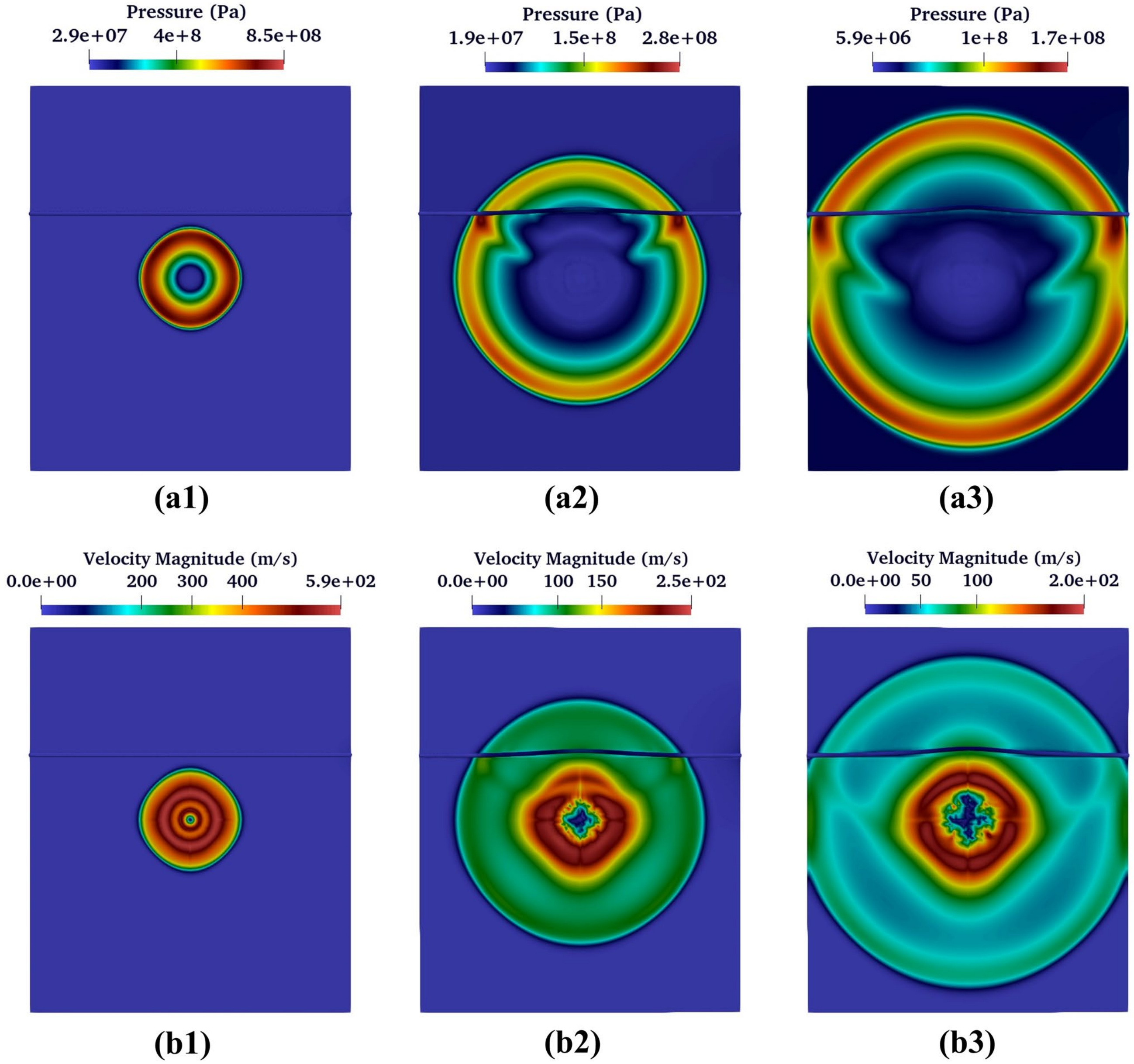

Fig. 15 Spatial distribution of the stress tensor components of the steel plate subjected to underwater explosion

component on the x-y plane is symmetric with respect to the line $x = y$. The stress tensor component on the y-z plane exhibits symmetry with respect to the line $x = 0$. The maximum value of the stress component on the x-y plane is 450 MPa. Overall, the stress distribution on the steel plate surface is smooth without any spikes, indicating that that developed FVM–SPH solver is capable of providing high-precision results when handling complex mechanical problems, especially in capturing stress variations without generating unnatural sharp fluctuations or noise.

The temporal evolution of the velocity distribution of the steel structure subjected to underwater explosion at 2.5, 4.0, 5.0, and 7.5 ms is shown in Fig. 18. After the ignition of the explosive, the shock wave propagates in the water medium. At time 1.5 ms, the shock wave impacts the steel plate, and the plate begins to deform. Since part of the internal energy is transferred to the kinetic energy of the steel plate, it can be found that the velocity magnitude of the steel plate increases rapidly to around 150 m s^{-1} (see Fig. 18). After the velocity magnitude of the steel plate reaches the maximum value, the velocity decreases gradually. The numerical results show that the developed FV-SPH method can provide a good prediction of the damage of solid structures under nearby underwater explosion.

The temporal evolution of the displacement at the center of the top surface of the steel plate is shown in Fig. 19.

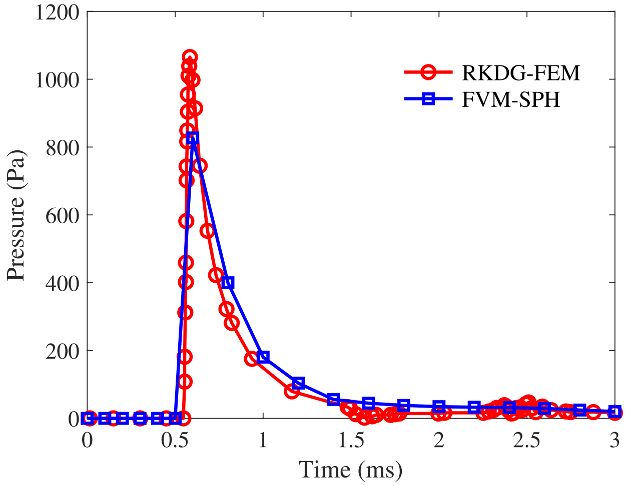

Fig. 16 Temporal evolution of the pressure at typical point subjected underwater explosion

At 0.6 ms, the shock wave impacts the plate. As part of the internal energy from the explosive is transferred to the kinetic energy of the steel plate, the displacement begins to increase significantly after 0.8 ms. Once the displacement reaches its maximum magnitude, it gradually stabilizes, approaching a steady state. For validation, the temporal evolution of the steel plate's deformation is compared with numerical results obtained using a combined RKDG-FEM approach [22], which shows general agreement. This comparison demonstrates the accuracy of the current simulation approach. Additionally, further numerical studies will be conducted to explore the deformation of composite structures subjected to 3D underwater shock loading, expanding the scope of the analysis in future work.

5.4 Damage of reinceforced concrete slab under blast loading

The three-dimensional damage of a reinforced concrete slab under TNT explosive detonation is simulated to further validate the fluid–structure interaction and the calculation of the external force applied to SPH particles. As described in Eq. (35), the external force is determined based on the mass flux increments of different phases. The initial configuration of the reinforced concrete slab and blast loads is shown in Fig. 20, which is identical to the experimental setup in [41]. The dimensions of the reinforced concrete slab are 1.0 m × 1.0 m × 0.04 m, with steel reinforcement having a length of 1.0 m and a diameter of 0.006 m. The distance between the steel reinforcements is set at 0.075 m. The air domain is discretized using FVM, while the solid structure is modeled with SPH particles. For the fluid domain, symmetrical boundary conditions are applied on the planes $x = 0$, $y = 0$, and $z = 0$, with non-reflecting boundary conditions applied to the remaining boundaries. For the reinforced concrete, symmetrical boundary conditions are applied to the planes $x = 0$ and $y = 0$. The top and bottom surfaces are treated as free boundaries, and the back two boundaries are fixed. The

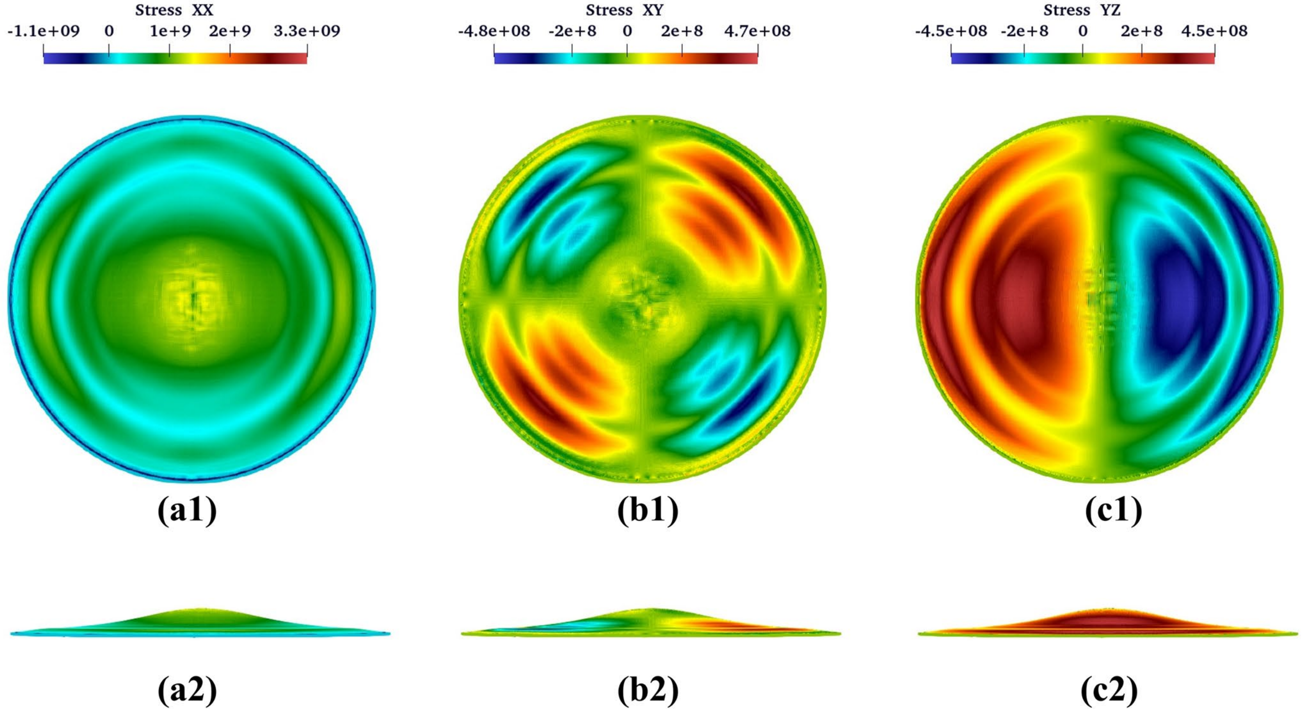

Fig. 17 Top view (**a1–c1**) and side view (**a2–c2**) of the spatial distribution of the stress tensor components of the steel plate subjected to underwater explosion

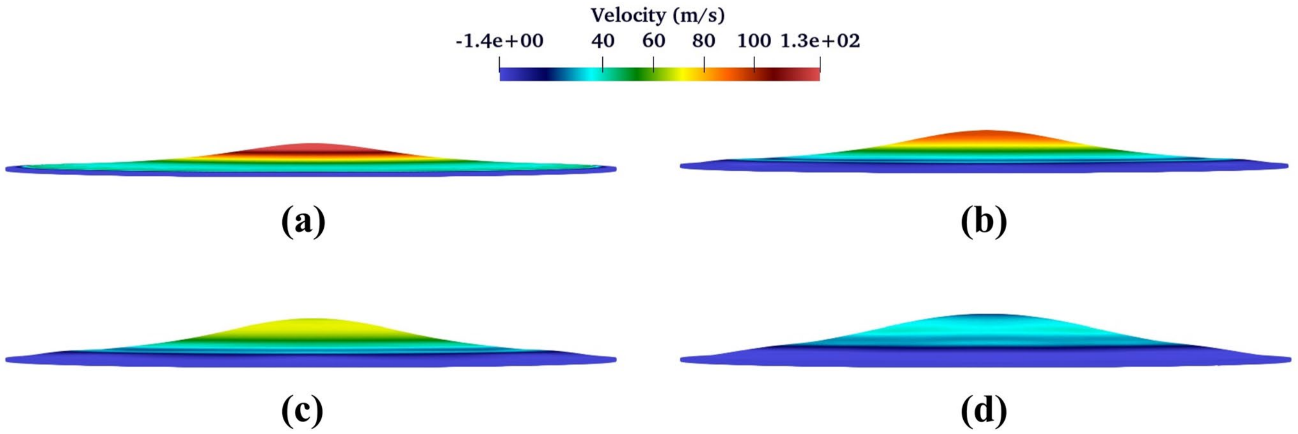

Fig. 18 Temporal evolution of the velocity distribution of the steel plate subjected to underwater explosion at 2.5, 4.0, 5.0, and 7.5 ms

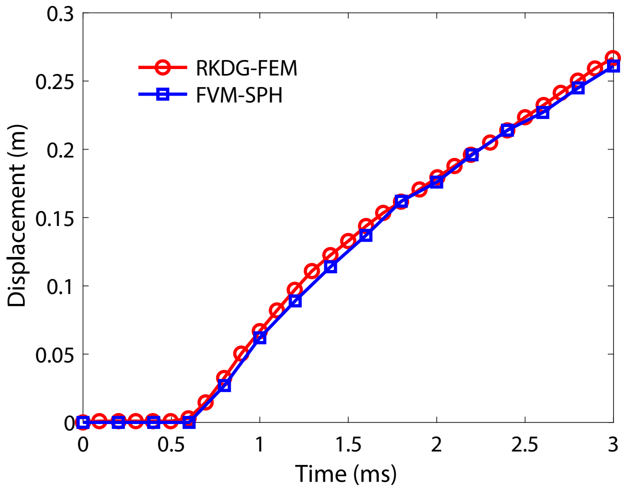

Fig. 19 Temporal evolution of the displacement of the center point at the top surface of the steel plate using the the developed FVM–SPH solver and RKDG-FEM method [22]

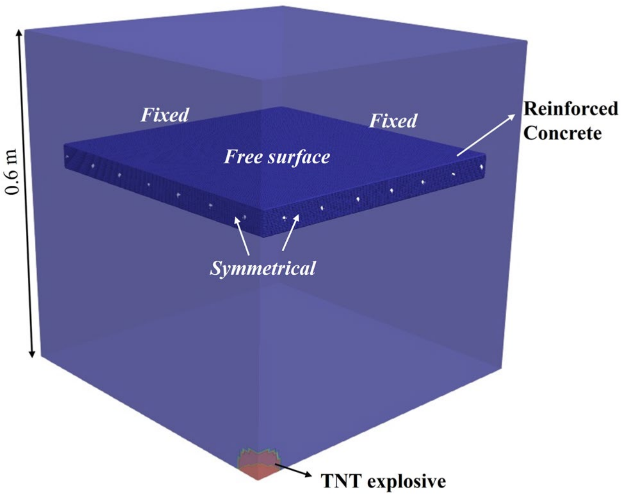

Fig. 20 The initial configuration of the damage of reinforced concrete slab under blast loading

initial particle spacing is 0.006 m, and a total of 640,001 particles are used in this numerical case. The initial mesh size is 0.0025 m. The parameters of the HJC and Johnson-Cook constitutive models, along with the Grüneisen EOS for modeling the dynamic behavior of reinforced concrete, are summarized in Tables 4, 5, and 6. The parameters for the JWL EOS of the TNT explosive are provided in Table 7.

We first simulated the TNT explosive detonation in the air medium to verify the implementation of the two-phase FVM solver for solving ideal explosive detonation problems. The temporal evolution of the total energy, pressure, and shock wave velocity propagation at different times (80, 120, 160, and 240 μs) is shown in Fig. 21. The results demonstrate that the developed two-phase FVM method effectively reproduces explosive detonation and shock wave propagation. Furthermore, we simulated the response of reinforced concrete slabs under close-in blast loading to analyze the damage modes and mechanisms of the structure, comparing the numerical predictions with experimental data from Wang et al. [41]. The damage to the reinforced concrete caused by shock wave propagation at times 140, 180, 240, and 300 μs is shown in Fig. 22. After the TNT explosive is ignited, the shock wave propagates through the air medium. When the shock wave reaches the bottom surface of the reinforced concrete, some of the internal energy is transferred to the kinetic energy of the concrete, causing the concrete to crack. The damage coefficient distribution of the reinforced concrete slab under blast loading, obtained from the GPU-accelerated multi-material FVM–SPH method, is shown in Fig. 23. Several cracks in both radial and circumferential directions are generated. The numerical damage contours of the reinforced concrete quarter-section, on both the top surface (a–e) and the bottom side (g), obtained using the multi-material FVM–SPH method, show good overall agreement with the experimental data (top surface (f) and the bottom side (h)) [41]. The present concrete model does not fully reproduce the tensile cracking and surface damage

Table 4 Johnson-Cook model parameters of steel [19]

A (MPa)	*B* (MPa)	*C*	*n*	*k*	T_{room} (K)	T_{melt} (K)
792	510	0.014	0.26	1.03	273	1793

Table 5 Parameters used for the Mie-Grüneisen EOS for steel [33]

ρ_0 (kg m^{-3})	C_0 (km s^{-1})	S_1	S_2	S_3	γ	α	E_0 (J)
7830	4.569	1.49	0	0	2.17	0.46	0

Table 6 Parameters of the HJC model for the concrete structure [33]

Basic parameters	Value	Strength parameters	Value	Damage parameters	Value	EOS parameters	Value
ρ_0 (kg m^{-3})	2,700	A	0.79	D_1	0.04	$p_{crush}(MPa)$	16
$G(GPa)$	28.0	B	1.60	D_2	1.00	μ_{crush}	0.001
$f_c(MPa)$	39.5	N	0.61	e_{fmin}	0.0008	$p_{lock}(GPa)$	0.80
		C	0.007	T(MPa)	4.2	μ_{lock}	0.10
		$\dot{\varepsilon}_0$	1.0			$K_1(GPa)$	85
		s_{max}	7.00			$K_2(GPa)$	−171
						$K_3(GPa)$	208

Table 7 Coefficients of the JWL model for TNT explosive [33]

ρ_0 (kg m^{-3})	*A* (Pa)	*B* (Pa)	R_1	R_2	*w*	E_0 (J kg^{-1})
1630	3.712×10^{11}	3.21×10^{9}	4.15	0.95	0.3	4.29×10^{6}

observed on the top face. Ongoing work focuses on developing and implementing more advanced cracking treatment methods to better capture complex fracture behavior in the concrete medium. In addition, as illustrated in Table 8, we also compared the numerical deflection of the center point of the reinforced concrete with the experimental data, it is found that the relative error is less than 15%, indicating that the GPU-accelerated FVM–SPH methodology is highly effective at capturing explosive detonation, shock wave propagation, and the deformation and damage of solid structures induced by shock wave propagation.

5.5 Dynamic fracture of steel tube under shock loading

The last strong fluid–structure interaction case used to validate the coupling of the FVM and SPH methods and check the robustness of the developed FVM–SPH solver is the 2D dynamic fracture of a steel tube under shock loading. During the explosion, the shock wave compresses the surrounding metal structure, generating numerous structural fragments and creating multiple fluid–structure interaction interfaces. This complexity can lead to issues such as negative energy and density, potentially resulting in program termination during simulation. Therefore, this case is designed to evaluate the effectiveness of the developed FVM–SPH solver in handling fluid–structure interactions between the explosive shock wave and high-speed moving debris. The dynamic fracture of a steel tube driven by the expansion of explosive gaseous products and shock wave propagation has been extensively studied by several researchers [21, 42]. For example, Libersky et al. [42] examined fragment patterns and mass distribution of metal materials using the SPH method. The simulation of dynamic fracture in steel tubes under blast loading involves fracture and fragmentation of materials, which is challenging for mesh-based methods. Techniques such as element erosion or element death in grid methods can lead to significant mass loss, negative density, and negative volume. In our current research, the developed FVM–SPH method is used to predict the physical process of dynamic fracture in a steel tube under blast loading.

As shown in Fig. 24, a quarter of the steel tube under blast loading is modeled in this study. For the fluid domain, symmetrical boundary conditions are applied to the left and bottom boundaries, and outlet boundary conditions are applied to the right and top boundaries. For the solid domain, the left and bottom sides of the steel tube (modeled using SPH particles) are treated with symmetrical boundary conditions. To replicate the experiment from [42], the air and explosive domains are discretized using a uniform structured mesh, while the steel tube is discretized using SPH particles. As depicted in Fig. 24, the radius of the explosive is set to 30 mm, and the thickness of the steel tube is 4 mm. The JWL EOS is applied to model the TNT explosive detonation, while the ideal gas EOS is used for the air medium. For material strength, the Johnson-Cook strength model in conjunction with the Mie-Grüneisen EOS is used to predict the dynamic behavior and fracture of the steel. The parameters

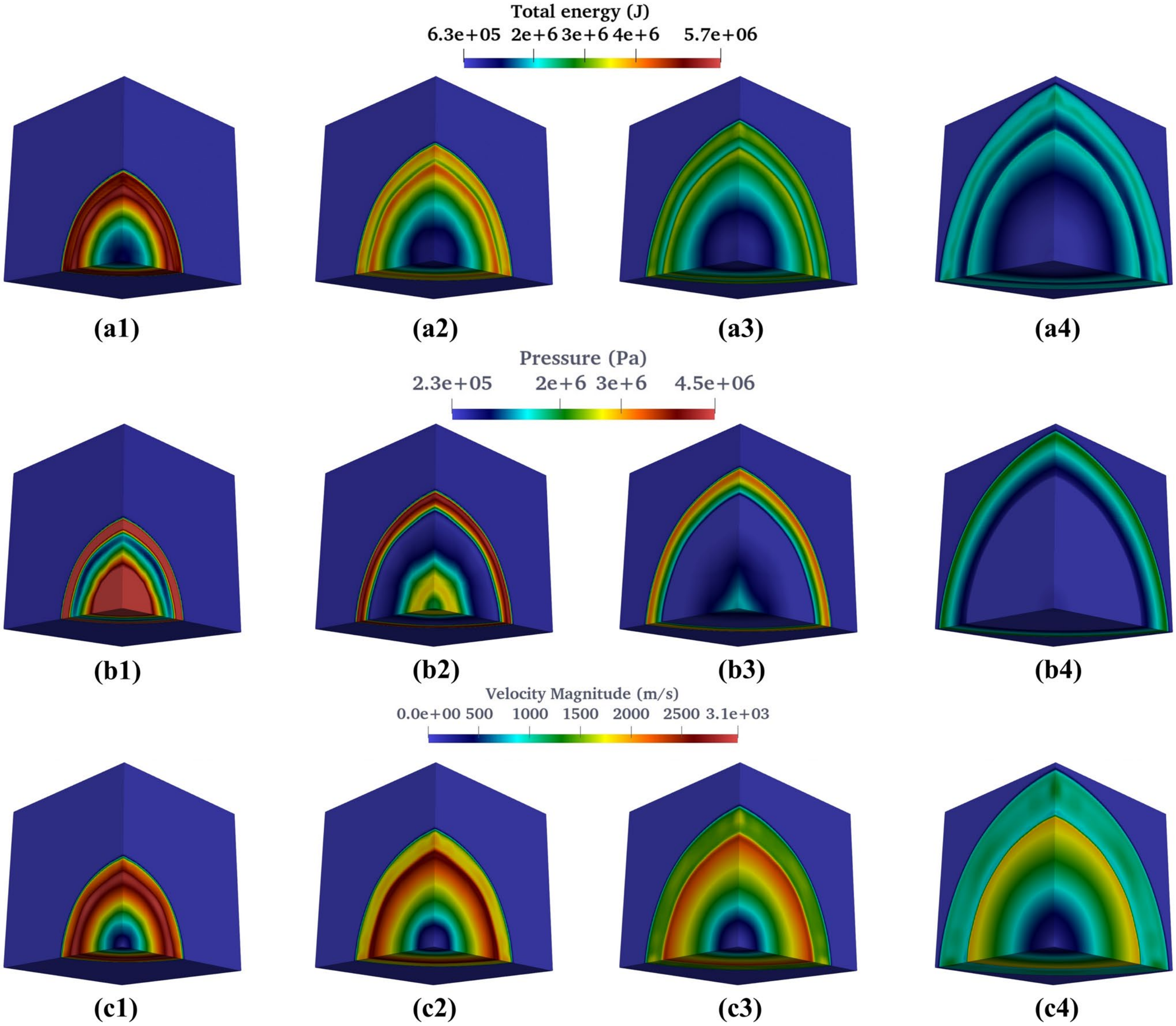

Fig. 21 The temporal evolution of the total energy, pressure, and velocity distributions of the 3D TNT explosive detonation in the air medium using multi-material FVM–SPH

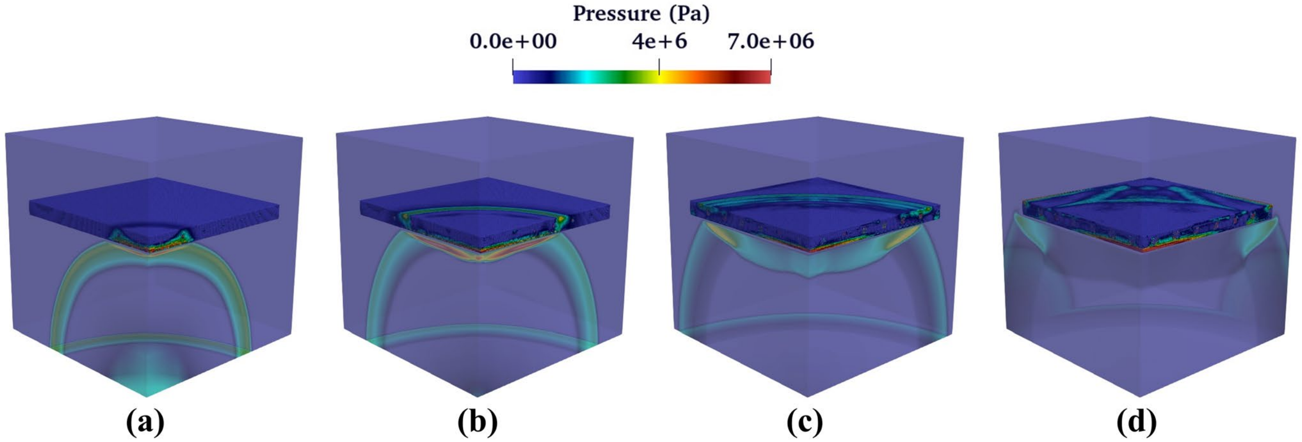

Fig. 22 The physical process of the shockwave propagation and its damage to nearby concrete

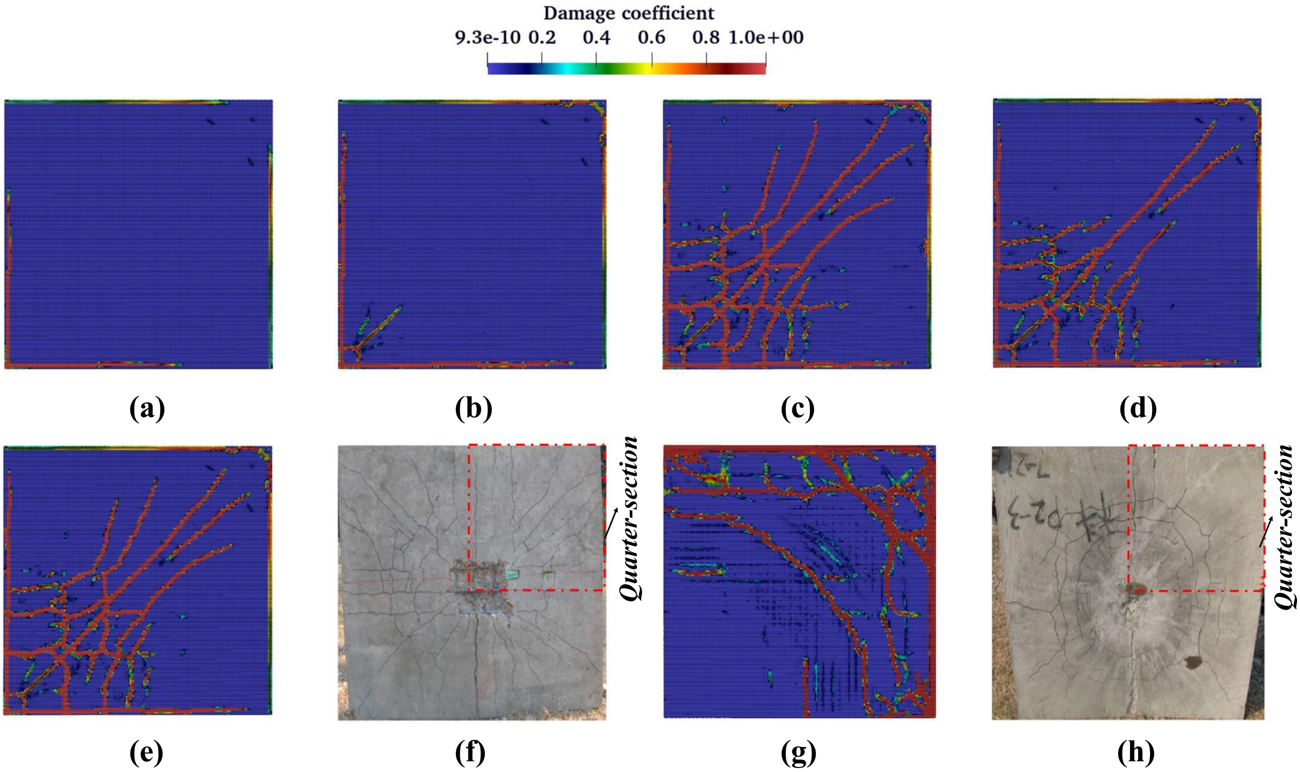

Fig. 23 Comparison of the temporal evolution of damage distribution in a quarter-section of reinforced concrete obtained from the FVM–SPH solver and experimental data [41]

Table 8 A comparison of the numerical results for the reinforced concrete obtained from the FVM–SPH solver with those measured experimentally by [41]

Damage (mm)	Computation	Experiment	Discrepancy (%)
Center deflection	30.6	35	12.5

for the Johnson-Cook model, and the JWL EOS are summarized in Tables 4, 5, and 7.

The temporal evolution of dynamic fracture in a steel tube under blast loads is shown through snapshots at various times—10, 20, 40, and 60 μs—in Fig. 25. Following the ignition of the explosive, the steel tube undergoes

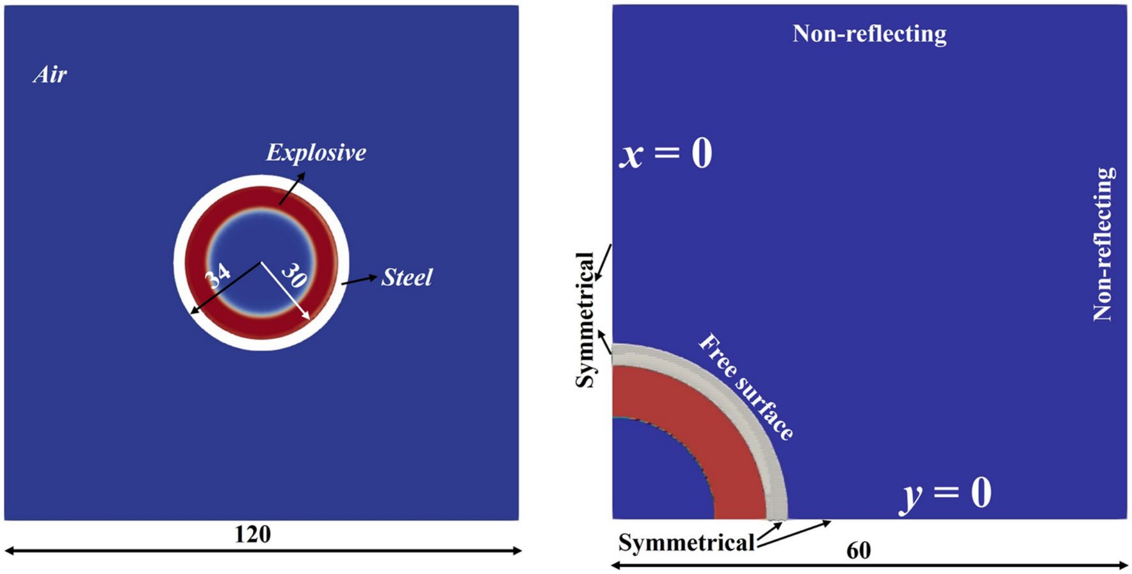

Fig. 24 Initial configuration of the dynamic fracture of steel tube under the expansion of explosive gaseous products and shock wave propagation. All of the dimensions are in mm

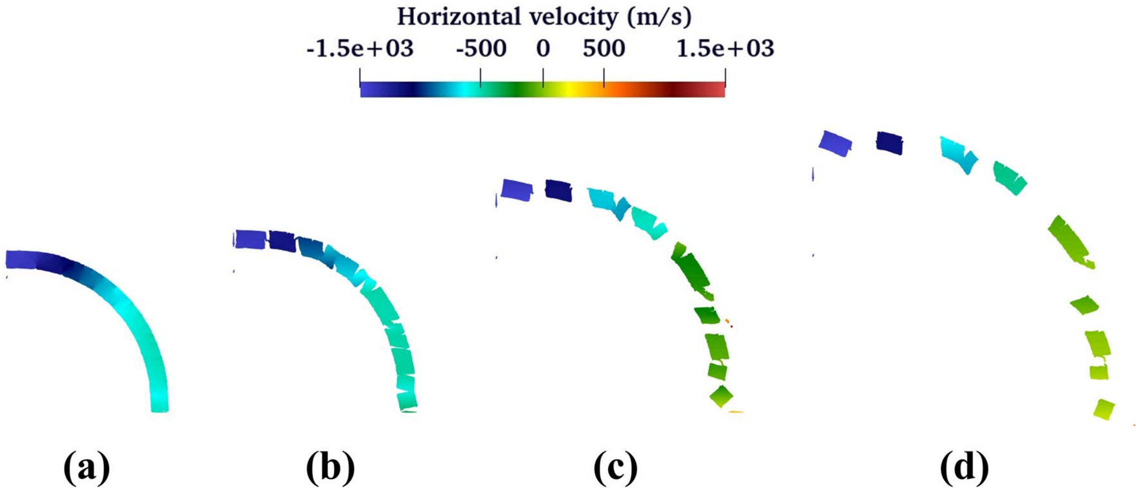

Fig. 25 The temporal evolution of the fragment distribution of the steel tube at different times 10, 20, 40, and 60 μs

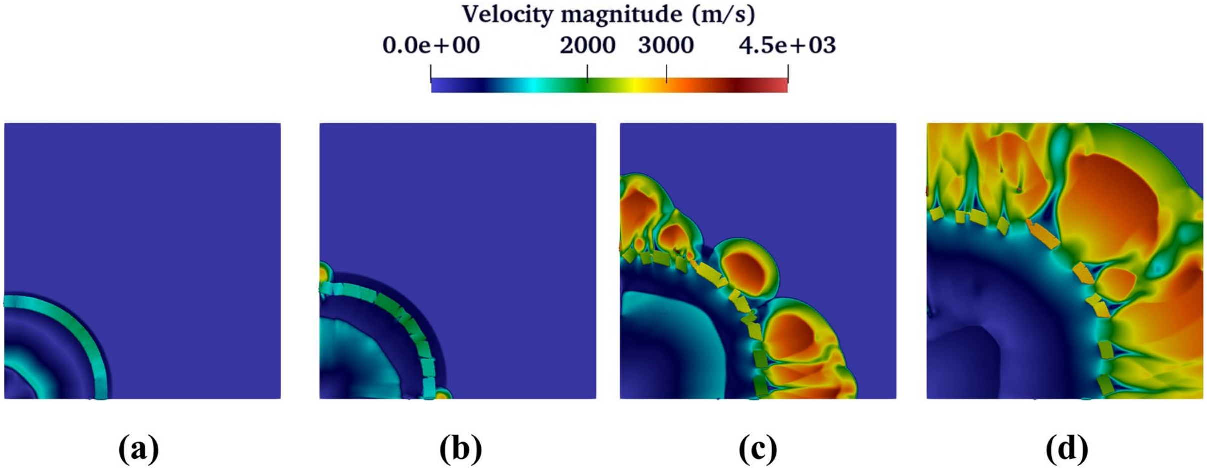

Fig. 26 The velocity distribution of the steel tube subjected to blast loading at different times 10, 20, 40, and 60 μs

compression due to the shock wave and the expanding gaseous products. The figure illustrates the progression of fracture in the steel tube, resulting from a combination of shear and tensile stresses. It can be observed that the maximum velocity magnitude of the fragments reaches around 1000 m s^{-1}.

The velocity distribution of the dynamic fracture at different time intervals—10, 20, 40, and 60 μs—is presented in Fig. 26. The developed FVM–SPH solver effectively captures key physical phenomena such as shockwave propagation, reflection, fragmentation of the steel tube, and pressurized gas leakage. In comparison with results from the pure meshless MPM (Material Point Method) approach used in [33, 43], the multi-material FVM–SPH method offers a better prediction of shock wave sharpness, pressure relief, and gas leakage. This improvement arises from the fact that the pure meshless approach neglected the surrounding air medium to simplify the initial modeling and enhance computational efficiency. As shown in Table 9, the relative errors are all less than 15 %, indicating that the average width and length of the steel tube fragments are in good agreement with experimental data from [44] (calculated using Error = $\frac{|\text{Experiment-Simulation}|}{\text{Experiment}}$). The average value of the thickness and length can be determined using $\left(\sum_{i=1}^{N} L_i\right)/N$, where N is the total number of fragments; L_i is the thickness or length of the ith fragment.

Table 9 Comparison of the numerical results and experimental data [44] in terms of the average width and thicknesses of the fragments

	Simulation	Experiment	Error
Width	7.23 mm	7.86 mm	8%
Thickness	3.7 mm	3.3 mm	12%

Additionally, the temporal evolution of total energy, kinetic energy, and internal energy of the steel tube is depicted in Fig. 27. After the shock wave impacts the cylindrical steel tube, the internal energy of the explosive is converted into the kinetic energy of the steel tube fragments, causing the kinetic energy to rapidly increase to 0.52 MJ. Simultaneously, the internal energy of the steel tube decreases. After 60 μs, the total and kinetic energy stabilize and maintain nearly constant values. This case demonstrates that the developed GPU-accelerated FVM–SPH method can effectively reproduce the dynamic fracture of a steel tube under blast loads.

6 Conclusion

In this paper, a GPU-accelerated multi-material FVM–SPH framework coupled with the immersed boundary method (IBM) has been developed to simulate shock wave propagation and its interaction with solid structures. The solver was rigorously validated through five benchmark cases: shock–bubble interaction, 2D/3D underwater explosions, blast-induced damage to reinforced concrete slabs, and dynamic fracture of steel tubes. The methodology integrates the finite volume method (FVM) for resolving compressible fluid dynamics and smoothed particle hydrodynamics (SPH) for capturing large structural deformations, with IBM enabling seamless two-way coupling to address challenges in fluid–structure interaction (FSI), such as pressure equilibrium and momentum transfer. Notably, the GPU-accelerated implementation achieved a 350× speedup over CPU-based SPH, allowing efficient simulations at scales involving millions of nodes and particles while preserving numerical stability. To the authors' knowledge, this work represents the first unified framework combining multi-material FVM, SPH, and IBM for high-fidelity modeling of explosive detonation, shock propagation, and structural damage.

Validation results demonstrated strong quantitative agreement with experimental data. The solver successfully reproduced complex phenomena such as shock reflection/refraction, cavitation in underwater explosions, and fracture propagation in metals, underscoring its capability for multiphase, multi-material problems. These outcomes highlight the framework's practical relevance for defense and engineering applications, such as evaluating blast resistance of infrastructure or optimizing containment designs for hazardous materials.

Although the present FVM–SPH framework shows promise in modeling shock–structure interactions, several limitations must be acknowledged. First, the FVM–SPH coupling introduces inherent numerical diffusion and interface inconsistencies, especially near complex boundaries. While the immersed boundary method partially mitigates this issue, future refinements are needed to reduce spurious oscillations and improve conservation. Second, the method remains computationally expensive for large-scale 3D problems requiring high resolution, a cost exacerbated by frequent particle-mesh data exchange. This may limit applicability to real-time or large-domain simulations. Third, the treatment of material failure and fracture in the SPH component is simplified; more sophisticated constitutive models are required for realistic damage prediction.

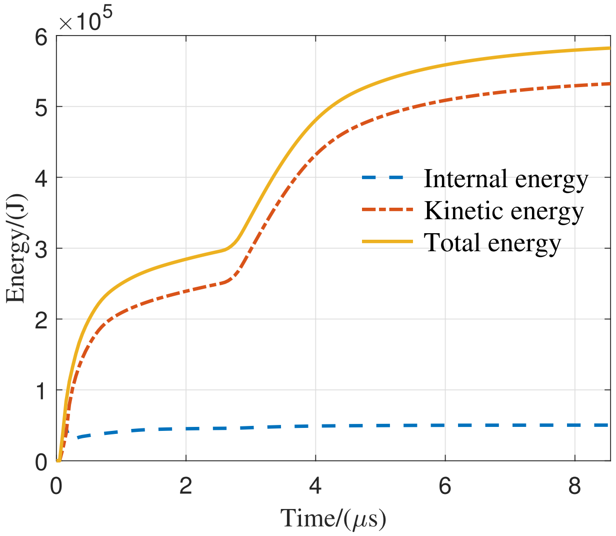

Fig. 27 Temporal evolution of the total energy, kinetic energy, and internal energy of the steel tube subjected to blast loading

Future work will focus on extending the methodology to address more complex scenarios. This includes implementing advanced constitutive models for heterogeneous materials (e.g., anisotropic composites, strain-rate-dependent ceramics) to improve damage prediction in composite structures, as well as investigating explosive-driven granular jets and their interaction with armored surfaces. Additionally, adaptive resolution techniques could be integrated to enhance computational efficiency in localized deformation zones, while experimental benchmarking using high-speed imaging and pressure sensors would further validate transient FSI predictions. By bridging computational mechanics with real-world applications, this framework establishes a foundation for advancing simulations in aerospace, marine engineering, and hazard mitigation, offering transformative potential for understanding and mitigating extreme fluid–structure interactions.

Appendix A: EOSs and constitutive models

Appendix A.1: Grüneisen equation of state

The Grüneisen EOS is used to describe the thermodynamic properties of materials under varying pressure and temperature conditions. This EOS is particularly useful in modeling high-temperature and high-pressure systems, such as shock waves or in understanding the behavior of materials in extreme conditions.

$$p = \begin{cases} \frac{\rho_0 C_0^2 \mu[1+(1-\frac{\gamma}{2})\mu-\frac{\alpha\mu^2}{2}]}{[1-(S_1-1)\mu-\frac{S_2\mu^2}{\mu+1}-\frac{S_3\mu^3}{(\mu+1)^2}]^2} + (\gamma+\alpha\mu)E & \mu > 0 \\ \rho_0 C_0^2 \mu + (\gamma+\alpha\mu)E & \mu \leq 0 \end{cases} \tag{A.1}$$

where $\mu = \frac{\rho}{\rho_0} - 1$, ρ_0 is the initial density, E is the current specific internal energy. γ, α, S_1, S_2, S_3 and C_0 are the coefficients of the material.

Appendix A.2. Elastic-perfectly plastic constitutive model

The elastic-perfectly plastic constitutive model is employed within the GPU-accelerated FVM–SPH solver to simulate and predict the dynamic behavior of metallic materials. To ensure that the material response remains independent of the reference frame, the Jaumann rate of the Cauchy stress is used. The Jaumann rate is a frame-independent measure of stress rate, which effectively accounts for rotations and deformations in the material without introducing spurious effects due to the choice of coordinate system. This is especially important in simulations of high-strain-rate phenomena where the material undergoes significant deformation, such as in impact or shock-wave simulations.

$$\dot{S}^{\alpha\beta} = \dot{S}_J^{\alpha\beta} + S^{\alpha\gamma}\dot{w}^{\beta\gamma} + S^{\gamma\beta}\dot{w}^{\alpha\gamma}. \tag{A.2}$$

The components of trial elastic deviatoric stress $S_e^{\alpha\beta}$ can be determined on the basis of Eq. (A.2) and Hook's law,

$$S_e^{\alpha\beta} = \Delta t \left(2G \left(\dot{\varepsilon}^{\alpha\beta} - \frac{1}{3}\delta^{\alpha\beta}\dot{\varepsilon}^{\gamma\gamma} \right) + S^{\alpha\gamma}\dot{w}^{\beta\gamma} + S^{\gamma\beta}\dot{w}^{\alpha\gamma} \right) + S_{(n)}^{\alpha\beta}, \tag{A.3}$$

where $S_{(n)}^{\alpha\beta}$ is the component of deviatoric stress at nth time step. The second invariant J_2 of the deviatoric part of the elastic trial stress $S_e^{\alpha\beta}$ is

$$J_2 = \frac{1}{2} S_e^{\alpha\beta} S_e^{\alpha\beta}. \tag{A.4}$$

This model assumes that the material exhibits elastic behavior up to a certain yield stress σ_Y, beyond which it undergoes perfectly plastic deformation without hardening,

$$S^{\alpha\beta} = \begin{cases} S_e^{\alpha\beta}, & \text{if } J_2 \leq \sigma_Y^2/3; \\ \sqrt{\frac{\sigma_Y^2}{3J_2}} S_e^{\alpha\beta}, & \text{if } J_2 > \sigma_Y^2/3. \end{cases} \tag{A.5}$$

in which J_2 is the second invariant of the stress tesnor. The Johnson-Cook visco-plastic constitutive model, which accounts for large strains, high strain rates, and elevated temperatures, is employed to describe the plastic behavior of metal materials under dynamic loading conditions.

$$\sigma_Y = \left[A + B(\varepsilon_p)^n \right] \left[1 + C \ln \left(\frac{\dot{\varepsilon_p}}{\dot{\varepsilon_0}} \right) \right] \left[1 - (T^*)^k \right], \tag{A.6}$$

The dimensionless temperature T^* is determined by

$$T^* = \frac{T - T_{\text{room}}}{T_{\text{melt}} - T_{\text{room}}}, \tag{A.7}$$

where T, T_{room}, and T_{melt} are temperature, room temperature, and melt temperature, respectively.

Appendix 3: HJC concrete model

The Holmquist-Johnson-Cook (HJC) constitutive model, developed by Holmquist, Johnson, and Cook [45], is well-suited for describing the dynamic behavior of concrete and similar brittle materials subjected to large strains, high strain rates, and high pressures. The normalized equivalent stress is defined as

$$\sigma_y^* = \frac{\sigma_y}{f_c} \tag{A.8}$$

where σ_y is the actual equivalent stress; f_c is the quasi-static uniaxial compressive strength. The specific expression for normalized equivalent stress is

$$\sigma_y^* = [A(1-D) + Bp^{*N}](1 + Cln\dot{\varepsilon}^*) \tag{A.9}$$

where D is the damage $(0 \leq D \leq 1.0)$; $p^* = p/f_c$; $\dot{\varepsilon}^* = \dot{\varepsilon}/\dot{\varepsilon}_0$ is the dimensionless strain rate; A, B, C, N are material constants. This HJC constitutive model accumulates damage from both plastic volume strain $\Delta\mu^p$ and equivalent plastic strain $\Delta\varepsilon^p$, and is expressed as,

$$D = \sum \frac{\Delta\varepsilon^p + \Delta\mu^p}{\varepsilon_f^p + \mu_f^p} \tag{A.10}$$

$$\varepsilon_p^f + \mu_p^f = D_1(p^* + T^*)^{D_2} \tag{A.11}$$

where D_1 and D_2 are constants; $T^* = T/f_c$, T is the maximum tensile hydrostatic pressure the material can withstand. The pressure in the three different regions (linear elastic region, transition region, and fully dense region) can be determined based on the volumetric strain.

Acknowledgements This work is financially supported by the National Natural Science Foundation of China (#12202203, #52439001), and the Research Grants Council of Hong Kong (Nos. GRF 16203123, 16208224, 16217225, CRF C7085-24 G, RIF R6008-24, TRS

T22-607/24N, and T22-606/23-R).

References

1. Saurel R, Petitpas F, Berry RA (2009) Simple and efficient relaxation methods for interfaces separating compressible fluids, cavitating flows and shocks in multiphase mixtures. J Comput Phys 228(5):1678–1712
2. Børvik T, Hanssen AG, Langseth M, Olovsson L (2009) Response of structures to planar blast loads-a finite element engineering approach. Comput Struct 87(9–10):507–520
3. Zakrisson B, Wikman B, Häggblad H (2011) Numerical simulations of blast loads and structural deformation from near-field explosions in air. Int J Impact Eng 38(7):597–612
4. Yin ZY, Chen XW (2023) Numerical study on the dynamic fracture of explosively driven cylindrical shells. Defence Technol 27:154–168
5. Wang C, Ding JX, Shu CW, Li T (2016) Three-dimensional ghost-fluid large-scale numerical investigation on air explosion. Comput Fluids 137:70–79
6. Sun ZX, Ni RC, Zeng ZX, Zhang X (2024) A localized subdomain smoothing MMALE particle method for efficient modeling FSI problems. Comput Methods Appl Mech Eng 419:116676
7. Feng RF, Fourtakas G, Rogers BD, Lombardi D (2024) A general smoothed particle hydrodynamics (SPH) formulation for coupled liquid flow and solid deformation in porous media. Comput Methods Appl Mech Eng 419:116581
8. Wang XD, Liu WK (2004) Extended immersed boundary method using FEM and RKPM. Comput Methods Appl Mech Eng 193(12–14):1305–1321
9. Silling SA, Lehoucq RB (2010) Peridynamic theory of solid mechanics. Adv Appl Mech 44:73–168
10. Yang CY, Zhu F, Zhao JD (2024) A multi-horizon fully coupled thermo-mechanical peridynamics. J Mech Phys Solids 191:105758
11. Yang CY, Zhu F, Zhao JD (2024) Coupled total-and semi-lagrangian peridynamics for modelling fluid-driven fracturing in solids. Comput Methods Appl Mech Eng 419:116580
12. Monaghan JJ (1992) Smoothed particle hydrodynamics. Ann Rev Astron Astrophys 30:543–574
13. Lucy LB (1977) A numerical approach to the testing of the fission hypothesis. Ast J 82:1013–1024
14. Liu MB, Liu GR, Lam KY, Zong Z (2003) Smoothed particle hydrodynamics for numerical simulation of underwater explosion. Comput Mech 30:106–118
15. Randles PW, Libersky LD (1996) Smoothed particle hydrodynamics: some recent improvements and applications. Comput Methods Appl Mech Eng 139(1–4):375–408
16. Feng DL, Liu MB, Li HQ, Liu GR (2013) Smoothed particle hydrodynamics modeling of linear shaped charge with jet formation and penetration effects. Comput Fluids 86:77–85
17. Chen JY, Peng C, Lien FS (2019) Simulations for three-dimensional landmine detonation using the SPH method. Int J Impact Eng 126:40–49
18. Chen JY, Feng DL, Lien FS, Yee E, Deng SX, Gao F, Peng C (2021) Numerical modelling of interaction between aluminium structure and explosion in soil. Appl Math Model 99:760–784
19. Chen JY, Feng DL, Sun QY, Peng C, Zhu YH, Yu SY (2023) Numerical modeling of shaped charge jet penetration into ceramic-metal double-layered medium using smoothed particle hydrodynamics. Int J Impact Eng 175:104526
20. Chen JY, Feng DL, Wang GY, Gao F, Peng C (2021) Numerical simulation of detonation and brisance performance of aluminized HMX using density-adaptive SPH. Propellants Explos Pyrotech 46(12):1800–1814
21. Tsuji P, Puso M, Spangler CW, Owen JM, Goto D, Orzechowski T (2020) Embedded smoothed particle hydrodynamics. Comput Methods Appl Mech Eng 366:113003
22. Ge L, Zhang AM, Wang SP (2020) Investigation of underwater explosion near composite structures using a combined RKDG-FEM approach. J Comput Phys 404:109113
23. Sun PN, Le T D, Guillaume O, Zhang AM (2021) An accurate FSI-SPH modeling of challenging fluid-structure interaction problems in two and three dimensions. Ocean Eng 221:108552
24. Guo C, Zhang HS, Qian ZH, Liu MB (2024) Smoothed-interface SPH model for multiphase fluid-structure interaction. J Comput Phys 518:113336
25. Lu Y, Liu CC, Wu PS, Luo L, Liu MB, Zhu C (2025) A novel SPH-based method for fiber orientation and detailed simulation of patient-specific vascular fluid-structure interactions. Comput Methods Appl Mech Eng 445:118196
26. Huang XP, Zhu B, Chen YM (2024) A coupled peridynamics-smoothed particle hydrodynamics model for fluid-structure interaction with large deformation. Phys Fluids 36:117131
27. Peskin CS (1972) Flow patterns around heart valves: a numerical method. J Comput Phys 10(2):252–271
28. Hérault A, Bilotta G, Dalrymple RA (2010) SPH on GPU with CUDA. J Hydraul Res 48(sup1):74–79
29. Mokos A, Rogers BD, Stansby PK, Domínguez JM (2015) Multi-phase SPH modelling of violent hydrodynamics on GPUs. Comput Phys Commun 196:304–316
30. Dehnen W, Aly H (2012) Improving convergence in smoothed particle hydrodynamics simulations without pairing instability. Mon Not R Astron Soc 425(2):1068–1082
31. Monaghan JJ (2005) Smoothed particle hydrodynamics. Rep Prog Phys 68(8):1703
32. Bui HH, Fukagawa R, Sako K, Ohno S (2008) Lagrangian meshfree particles method (SPH) for large deformation and failure flows of geomaterial using elastic-plastic soil constitutive model. Int J Numer Anal Meth Geomech 32(12):1537–1570
33. Ni RC, Li JS, Zhang X, Zhou X, Cui XX (2022) An immersed boundary-material point method for shock-structure interaction and dynamic fracture. J Comput Phys 470:111558
34. Toro EF (2013) Riemann solvers and numerical methods for fluid dynamics: a practical introduction. Springer, Berlin
35. Davis SF (1988) Simplified second-order Godunov-type methods. SIAM J Sci Stat Comput 9(3):445–473
36. Li L Q, Lohner R, Pandare A, Luo H (2021) Numerical modeling for compressible three-fluid flows with high explosive material. In: AIAA AVIATION 2021 FORUM, p. 2858
37. Haas JF, Sturtevant B (1987) Interaction of weak shock waves with cylindrical and spherical gas inhomogeneities. J Fluid Mech 181:41–76
38. Layes G, Le Métayer O (2007) Quantitative numerical and experimental studies of the shock accelerated heterogeneous bubbles motion. Phys Fluids 19(4):042105
39. Quirk JJ, Karni S (1996) On the dynamics of a shock-bubble interaction. J Fluid Mech 318:129–163
40. Peng C, Wang S, Wu W, Yu HS, Wang C, Chen JY (2019) LOQUAT: an open-source GPU-accelerated sph solver for geotechnical modeling. Acta Geotech 14:1269–1287
41. Wang W, Zhang D, Lu FY, Wang SC, Tang FJ (2013) Experimental study and numerical simulation of the damage mode of a square reinforced concrete slab under close-in explosion. Eng Fail Anal 27:41–51
42. Libersky LD, Randles PW, Carney TC, Dickinson DL (1997) Recent improvements in sph modeling of hypervelocity impact. Int J Impact Eng 20(6–10):525–532

43. Yang PF, Liu Y, Zhang X, Zhou X, Zhao YL (2012) Simulation of fragmentation with material point method based on Gurson model and random failure. Comput Model Eng Sci 85(3):207
44. Tang TG, Gu Y, Li QZ (2003) Expanding fracture of steel cylinder shell by detonation driving. Explos Shock Waves 23(6):529–533
45. Johnson GR, Stryk RA, Holmquist TJ, Beissel SR (1997) Numerical algorithms in a lagrangian hydrocode. Tech. rep, ALLIANT TECHSYSTEMS INC HOPKINS MN